



Unravelling the preservation of fault scarps in the Atacama Fault System, northern Chile: Insights from cosmogenic nuclides and topographic analysis

P. Rivera^{a,b,*}, G. González^{a,b}, S.A. Binnie^c

^a Programa de Doctorado en Ciencias mención Geología, Universidad Católica del Norte, Av. Angamos 0610, Antofagasta, Chile

^b Centro de Investigación para la Gestión Integrada del Riesgo de Desastres (CIGIDEN), Chile

^c Institute of Geology and Mineralogy, University of Cologne, Zülpicher Str. 49b, 50674, Cologne, Germany

ARTICLE INFO

Handling editor Claudio Latorre

Keywords:

Fault scarp degradation
Geomorphology
Tectonics
Quaternary
Atacama Fault System
Atacama desert
Northern Chile
Cosmogenic nuclides

ABSTRACT

Fault scarps are commonly used as temporary markers in palaeoseismological analysis, with their preservation controlled by the balance between slip and erosion rates. The northern Chile forearc, located in the core of the Atacama Desert, represents one of the driest settings on Earth, where mean annual rainfall is near zero and erosion rates are exceptionally low. Here, we investigate an anomalous case in the Atacama Fault System (AFS), northern Chile, where free faces have persisted for tens of thousands of years. To examine this balance, we focus on three branches of the AFS (Naguayán, Cerro Fortuna, and Salar del Carmen Faults), combining geomorphological mapping, ¹⁰Be-derived erosion rates, and sedimentological evidence. Our results indicate that the free faces have remained preserved for more than 14 ka despite a slow fault slip rate of ~0.07 mm yr⁻¹ and have retreated at an average rate of only ~0.03 m ka⁻¹. Scarp degradation is predominantly controlled by slow, diffusive processes, with the diffusion coefficient for the Salar del Carmen fault scarp calculated as $k = 0.063 \pm 0.018 \text{ m}^2 \text{ ka}^{-1}$. Localized channel incision across fault scarps has been triggered by sporadic high-intensity rainfall events, as evidenced by low catchment-mean erosion rates (~0.5–2.9 m Ma⁻¹) estimated from ¹⁰Be concentrations. The remarkable preservation of free faces is attributed to two main factors: extensive gypsic soil development and the prevalence of long-term hyperaridity. Minimal but significant moisture input from coastal fog promotes gypsic soil formation, enhancing moisture retention and driving gypsum cementation that stabilizes alluvial surfaces and prevents free face collapse. Sporadic rain events retain erosion rates in active catchments that are lower than the fault slip rate, allowing for scarp preservation. We propose a conceptual model in which the combined effects of (i) a hyperarid climate, (ii) sporadic but geomorphically effective hydrologic events, (iii) low tectonic slip rates, and (iv) salt-induced cementation act together to inhibit scarp degradation. These findings challenge conventional degradation and underscore the importance of evaluating surface processes in palaeoseismological interpretations, improving our understanding of fault activity, landscape evolution, and seismic hazard in hyperarid regions.

1. Introduction

Arid and hyperarid deserts worldwide as the Atacama, Negev and Namib (e.g., Houston, 2006; Begin, 1992; Enzel et al., 1996; Muir et al., 2023) are characterized by extremely low precipitation that results in minimal and sporadic surface run-off, thereby reducing erosion rates and promoting the long-term preservation of tectonic geomarkers over hundreds of thousands of years, even millions of years (Dunai et al., 2005). In these settings, landscape stability is sustained by relatively limited weathering, development of saline soils, and scarce rainfall, which together inhibit denudation and preserve landforms over long

timescales (e.g. Matmon et al., 2009; McFadden et al., 2000; Muir et al., 2023). Despite this recognition, the specific mechanisms controlling landscape preservation in deserts remain poorly constrained and often described in general terms. For instance, the role of soil mineralogical composition, such as gypsum and other salts, in inhibiting surface degradation and limiting runoff processes has not been systematically assessed, leaving a key gap in understanding how desert soils mediate the balance between tectonic activity and surface processes.

The northern Chile forearc is situated in the core of the Atacama Desert, which is among the driest regions on Earth, where mean annual rainfall is often <3 mm yr⁻¹ (Houston and Hartley, 2003; Houston,

* Corresponding author. Programa de Doctorado en Ciencias mención Geología, Universidad Católica del Norte, Av. Angamos 0610, Antofagasta, Chile.
E-mail address: prb012@alumnos.ucn.cl (P. Rivera).

2006). This hyperaridity, modulated by the Pacific Anticyclone, cold Humboldt Current, and orographic shadowing (Houston, 2006), suppresses fluvial incision and promotes exceptional preservation of morphological features by imposing extremely low erosion rates (Ewing et al., 2006; Amundson et al., 2012). Spatial variations in coastal fog and sporadic rains add complexity to the erosional processes (Cereceda et al., 2008). This erosion-limited western slope of the Andes contrasts with its eastern slope, at the same latitude, where the active landscape is dominated by fluvial incision and higher erosion rates (Montgomery et al., 2001; Norton and Schlunegger, 2011). The influence of a pronounced climatic and erosional gradient both along and across the Andes governs regional variations in weathering intensity, soil developed, vegetation cover (Carretier et al., 2018).

Whereas active tectonics in the northern Chile forearc is significantly dominated by plate convergence, several fault scarps related to the Atacama Fault System (AFS, Fig. 1, Arabasz, 1971) configure an extensional province that is tightly connected to the morphology of the Coastal Cordillera (e.g. Delouis et al., 1996; González et al., 2003). For more than ~1000 km between 21° and 25°S, this fault system is organized in several branches across the Coastal Cordillera and the Mejillones Peninsula. Its branches bound tilted blocks and basins, shaping a basin-and-range morphology with mountain front displacements of up to 500 m persisting for tens of kilometers. Along the piedmont of the mountain front, the main branches display fault scarps, attesting to the interplay between active tectonics and surface processes during the Quaternary (e.g. Delouis et al., 1996; González and Carrizo, 2003; Cortés et al., 2012; Ewiak et al., 2015). In this climatic context, scarps of the AFS retain free faces for >14 ka, as shown optically stimulated luminescence (OSL) dating and fault slip rate estimates of ~0.07 m/ka (Del Río et al., 2019; González et al., 2025). Such long-lived preservation is unusual, even compared to other arid settings like the Basin and Range or the Namib desert (e.g., Wallace, 1980), raising the question of whether their morphology primarily reflects active faulting or extreme climatic stability. Another striking feature of the AFS scarps is the widespread development of gypsic soils. Gypsum-rich horizons are diagnostic of pedogenesis under arid conditions and can record surface stability and long-term environmental conditions (Herrero and Porta, 2000; Rech et al., 2003). Comparative studies in other hyperarid regions, such as the Negev deserts, reveal similar gypsum accumulations formed over timescales of tens of thousands of years (Amit et al., 1995; Enzel et al., 1996; Gerson et al., 1993). The occurrence of these soils along fault scarps offers a valuable opportunity to evaluate landscape stability, soil formation processes, and their relationship with tectonic displacements. The preservation of normal fault scarps is commonly used as a temporary marker for paleoseismological analysis (e.g., Wallace, 1977; Pierce and Colman, 1986). However, their morphology reflects the competition between tectonic slip and surface processes (McCalpin, 2009). Scarps persist when fault slip exceeds erosion (e.g., DuRoss et al., 2022; Suter, 2015; Johnson et al., 2018) and degrade rapidly when erosion dominates (e.g., De Pascale et al., 2016; Chen et al., 2019). Understanding this balance is crucial for assessing the role of surface processes in normal fault scarp preservation and for evaluating the seismic hazard associated with active faults.

This study investigates the factors controlling the preservation of normal fault scarps in the AFS through (1) detailed geomorphic mapping and scarp morphology analysis, (2), stratigraphic characterization of scarp-derived deposits, (3) mineralogical analysis of gypsic soils, and (4) comparison of tectonic slip rates and catchment-mean erosion rates derived from cosmogenic ^{10}Be . We focus on three representative branches of the AFS near 23°S: (i) the southern section of the Naguayán Fault (NGF), (ii) the northern section of the Cerro Fortuna Fault (CFF), and (iii) the northern section of the Salar del Carmen Fault (SCF). We propose a conceptual model that synthesizes our findings to elucidate the long-term preservation of normal fault scarps in hyperarid landscapes.

2. Geomorphology and palaeoclimate

2.1. Geomorphology

The Coastal Cordillera between 23 and 24°S is a dominant large-scale morphological feature of northern Chile. Its western margin comprises a prominent coastal cliff and a widely spread coastal plain close to the Mejillones Peninsula (Fig. 1), whereas the inner part of the Coastal Cordillera is characterized by flat intermontane basins resulting from an intense period of erosion during the Cenozoic. The eastern margin of the Coastal Cordillera is a well-defined mountain front controlled by the tectonic activity of the Salar del Carmen Fault, while farther north it splits into a series of faults, resulting in a gradual transition from the range into the Central Depression (Hartley et al., 2005). This configuration has been shaped by the Quaternary tectonic activity of the AFS (Naranjo, 1987; Niemeyer et al., 1996), forming predominantly north-south to northeast-southwest fault-bounded basins, limited to the west by major faults and creating a half-graben-like morphology. In our study area (23°–24°S), persistent extensional deformation of the upper plate since the Miocene has facilitated the capture of fault-bounded subbasins within the Coastal Cordillera (Hartley et al., 2005). Within this setting, conspicuous fault scarps are preserved on Plio-Pleistocene surfaces along the piedmont, providing key markers of Quaternary tectonic activity. In some sectors fault scarps have been locally eroded or buried by sediments within major fluvial valleys that connect upstream catchments to local base levels.

2.2. Climate and palaeoclimate

At present, the hyperarid core of the Atacama Desert experiences annual precipitation of less than 3 mm per year (Houston, 2006), which is attributed to the cold upwelling water of the Peru-Chile current, the Hadley circulation, and the rain shadow effect of the Andes. Infrequent intense rainfall, influenced by austral westerlies, the El Niño-Southern Oscillation, and coupled variations in the SE Pacific anticyclone, generates anomalous precipitation events (e.g. Bozkurt et al., 2016; Ritter et al., 2019; Böhm et al., 2021; Reyers et al., 2023). Coastal fog (locally termed *camanchaca*), generated by the interaction of the SE Pacific anticyclone with the cold Peru-Chile current (Goudie et al., 2002) reaches altitudes of 800–1000 m a.s.l. and is a critical mechanism for salt transport and gypsum/anhydrite-rich soil formation (Rech et al., 2003; Wang et al., 2014).

Although various studies (Dunai et al., 2005; Rech et al., 2010, 2019; Ritter et al., 2018) have provided evidence of extreme aridity in the Atacama Desert since the mid-Miocene, the timing of the onset of hyperaridity remains a subject of debate. Previous works have shown that sedimentary clastic accumulation in the region (24°S) significantly decreased approximately 2.1 million years ago (Ewing et al., 2006; Amundson et al., 2012). This indicates that significant climate change occurred approximately 2.2–2.0 million years ago, which aligns with the onset of the Pacific El Niño-Southern Oscillation (ENSO) cycle (Wara et al., 2005). Pre-Quaternary, erosion and sedimentation processes connected upland bedrock and hillslopes with fluvial systems, potentially leading to the removal of hillslope sediments and the formation of extensive fan complexes near the end of the Pliocene (Jungers et al., 2013). Conversely, erosion and accumulation processes during the Pleistocene were markedly slower, with reduced stream incision and extensive salt formation, indicating an abrupt decrease in precipitation (Amundson et al., 2012). Available estimates indicate extremely low accumulation rates in areas adjacent to the study site ($\approx 2.1 \text{ m Myr}^{-1}$; Jungers et al., 2013).

3. Atacama fault system (AFS)

The AFS is the dominant structural element of the northern Chilean Coastal Cordillera. It extends more than 1000 km between latitudes 21°S

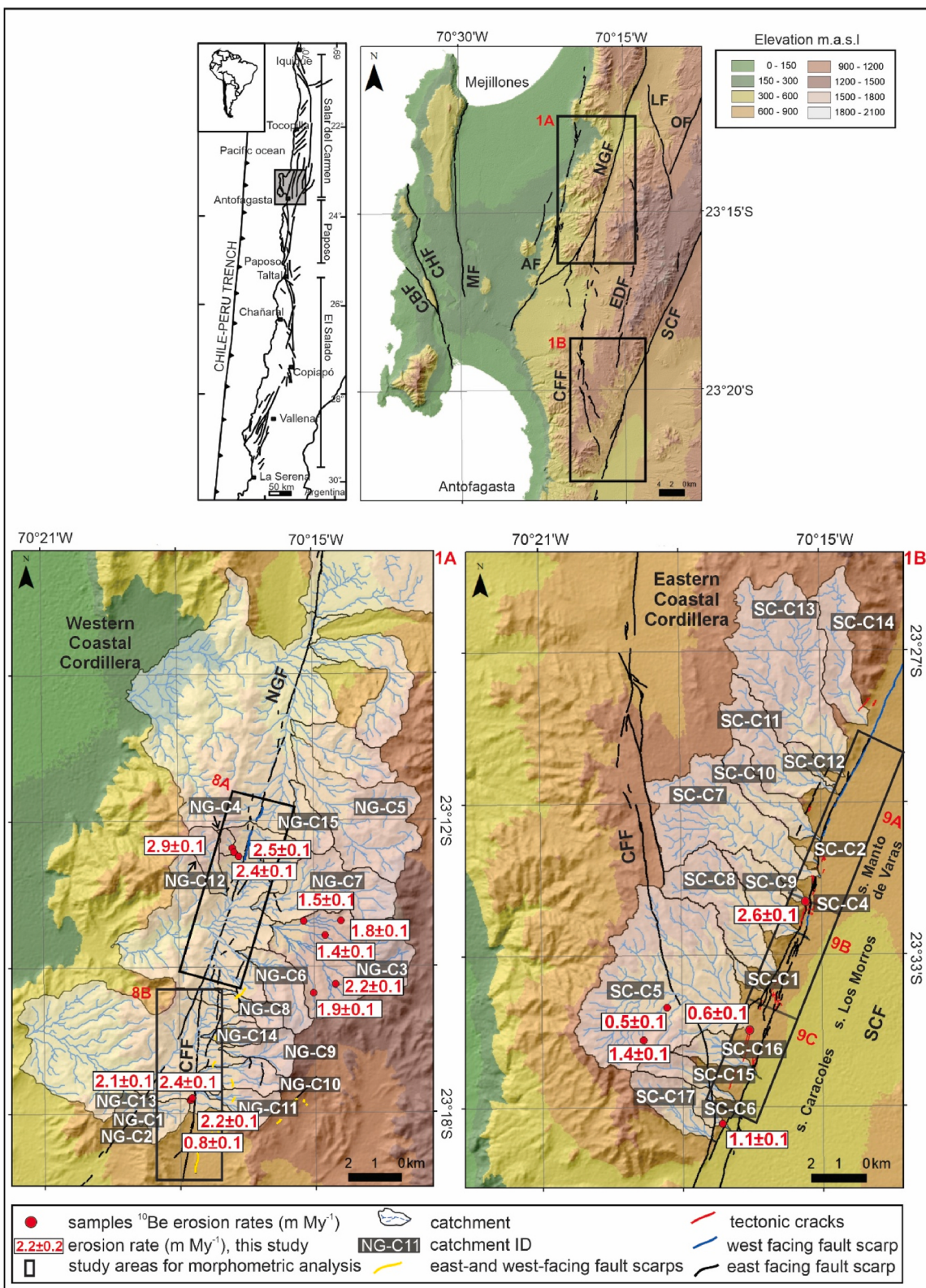


Fig. 1. (Upper left) Regional map of the Atacama Fault System (AFS), modified from Arabasz (1971). (Upper right) Digital elevation model (SRTM 30 m, obtained from <https://doi.org/10.5067/MEaSUREs/SRTM/SRTMGL1.003>), processed in ArcMap 10.8.2 (ESRI, proprietary license), showing fault-controlled mountain fronts (black lines) and fault acronyms showing fault-controlled mountain fronts (black lines) and fault acronyms: CBF = Caleta Bandurrias; CHF = Caleta Herradura; MF = Mejillones; AF = Aeropuerto; NGF = Naguayán; CFF = Cerro Fortuna; EDF = El Desesperado; LF = Laguna; OF = Ordóñez; SCF = Salar del Carmen. Rectangles indicate the study areas: (1A) Naguayán-Cerro Fortuna faults and (1B) Salar del Carmen Fault. Mapped fault scarps and main drainage catchments within the Coastal Cordillera are shown. Grey squares mark catchment IDs: white squares indicate ^{10}Be -derived erosion rates ($m \text{ Myr}^{-1}$); red circles denote sediment sampling sites. Dashed black lines outline subareas of detailed morphometric analysis: southern NGF, northern CFF, and SCF segments (Manto de Varas, Los Morros, Caracoles).

and 30°S and consists of three arched trench-parallel segments denominated from north to south as Salar del Carmen, Paposo, and El Salado (Fig. 1; Arabasz, 1971). The AFS was formed as a trench parallel strike-slip fault system by oblique subduction during the early Cretaceous (Scheuber and Andriessen, 1990; Scheuber and González, 1999). During the Cenozoic, extensional deformation (Delouis et al., 1998; González and Carrizo, 2003) reactivated several ~ NS branches of the AFS configuring the intermontane basins of the Coastal Cordillera. Later, during the Quaternary, metric-scale scarps formed in alluvial deposits (e.g., González et al., 2006). Among them, the Mejillones, Caleta Heradura, Mititus, and Salar del Carmen Faults have been broadly studied (e.g., Allmendinger and González, 2010). Surveys devoted to unravelling their upper-plate faulting activity have demonstrated the occurrence of 2–3 palaeo Mw 6–7 earthquakes during the Late Quaternary (Cortés et al., 2012) and slip rates not greater than ca. 0.07 mm yr⁻¹ (González et al., 2025).

4. Methods

4.1. Geomorphological surface characterization

To improve our understanding of the relationships between palaeo-surface abandonment and fault activity, we perform detailed-scale mapping (1:5000) that includes the identification of geomorphological surfaces and fault scarps along the piedmont of the Coastal Cordillera in the NGF, CFF, and SCF. To constrain the timing of palaeosurface preservation, we compiled published surface-exposure ages from González et al. (2006), Placzek et al. (2010), and Amundson et al. (2012). All ages were recalculated with CRONUS-Earth v3 (Balco et al., 2008) using LSDn scaling (Lifton et al., 2014), details in Supplementary Material, Table S6.

The criteria for geomorphic surface identification and mapping were based on Evenstar et al. (2017) and our field and remote observations using false-colour satellite images of the palaeosurfaces from Landsat-7 (red: band 7, green: band 4, blue: band 2) and digital elevation models (DEMs) with a spatial resolution of 3.5 cm/px (see next section). We used four main parameters and markers to characterize the surfaces: (1) topographic parameters (slope angle and slope direction), (2) the presence of desert pavement, (3) drainage network incision, and (4) soil development. Detailed stratigraphic observations, combined with new tephra ages measured in this study, were used to constrain the timing of depositional events and to characterize sedimentary processes within each study area. The tephra ages were determined using the ⁴⁰Ar/³⁹Ar radiometric dating method at the OSU Argon Geochronology Laboratory in Oregon, USA, which employs the single-crystal laser heating extraction technique.

4.2. Methodology of morphometric analysis

The morphometric analysis was structured into three main parts: (1) fault scarp degradation staging, (2) evaluation of erosion in the catchment upstream of a river that incises the fault scarp, and (3) catchment morphology analysis. In this paper, the term catchment refers to kilometre-scale drainage basins, including the main fluvial catchment where the principal river incises the fault scarp, and smaller subcatchments, which we define as metric-scale drainage basins within the larger catchment. High-resolution DEMs were generated through drone-based photogrammetry using the structure from motion (SfM) technique using Agisoft Metashape Professional, version 1.7.0.11701, proprietary license. An Inspire II unmanned aerial vehicle (UAV) was used for data acquisition, with control points recorded via a Trimble R4. These high-resolution DEMs were specifically employed to generate topographic profiles. In addition, a 30-m resolution DEM from the NASA Shuttle Radar Topographic Mission (SRTM) and TopoToolbox (Schwanghart and Scherler, 2014) in MATLAB R2023b (proprietary software).

To classify the degradation stage of each fault scarp, thirty-seven

topographic profiles were obtained for detailed analysis across the three study areas. Specifically, thirteen profiles for Salar del Carmen (SCF), nine profiles for Cerro Fortuna (CFF), and fifteen profiles for Naguayán (NGF) were analysed. Measurements were conducted five times in each domain of the scarp slope (free face, debris slope, and wash slope) and averaged to obtain a single representative value. From these profiles, the distribution of slopes was identified for the classification of degradation stages according to Wallace (1977), considering the far-field slope, including the presence or absence of a *free face*, *basal concavity*, and *crestal convexity*.

To evaluate fault scarp degradation with respect to the incision of streams across the fault, we developed the discontinuity index (Ds), which is defined as follows:

$$Ds = \frac{\sum_{i=1}^n (Li)}{Ls}$$

where Li is the length of a surface fault trace unaffected by transverse drainage systems and Ls is the length of the analysis window, which was set at 400 m for this study. This window, which represents approximately 10 % of the length of each analysed surface fault trace, enhances the data representation. Longer windows risk excessive smoothing, whereas shorter windows lead to high data discretization. Within this window, the length of the scarp was measured, and Ds was computed as the ratio of the cumulative scarp length (Li) to the window length ($Ls = 400$ m). This index quantifies the degree to which a scarp has been bisected by fault-transverse fluvial incision.

To standardize the statistical sample, (1) only scarps with lengths along strike greater than 50 % of the analysis window ($Ls > 200$ m) were included in the analysis, and (2) transfer zones between segments, which contribute to additional fault segmentation, were excluded. (3) The mode of the Ds values was selected to represent the fault section evaluated. The mode was determined based on interval groupings of Ds values in bins of 0.1. The Ds index was applied in our three study areas: (1) Salar del Carmen Fault (SCF): the sections analysed included the *Manto de Varas*, *Los Morros* and *Caracoles* segments as defined by González and Carrizo (2003); Naguayán Fault (NGF): *Naguayán* southern section; and (3) Cerro Fortuna Fault (CFF): *Cerro Fortuna* northern section. The Ds index provides valuable insight into the balance between the frequency of fluvial incision and active vertical tectonics. A Ds value of 1 indicates that the scarp is unaffected by transverse drainages, a condition typically observed when vertical displacement rates exceed the incision capacity of streams. In contrast, as the Ds values approach 0, enhanced dissection of the scarp by fluvial incision is observed, suggesting either comparatively lower slip rates or increased downcutting downstream of the catchments.

Catchment morphology was delineated on the basis of morphological parameters, including drainage patterns, orientation, slope gradient, and catchment area. Basin-scale variations were assessed through these metrics and the spatial distributions and geometries of the catchments were analysed to evaluate their relationships with structural controls and base-level changes. All these analyses were performed using ArcMap 10.8.2.

4.3. Cosmogenic ¹⁰Be

To assess fault scarp preservation within a broader framework of rates of landscape evolution, seven catchments were selected to determine regional erosion rates using concentrations of cosmogenic ¹⁰Be determined via AMS (Accelerator Mass Spectrometry).

4.3.1. Site selection

¹⁰Be concentrations in fluvial sediments can provide spatially averaged estimates of erosion in the upstream catchment area (Granger et al., 1996; Bierman and Steig, 1996). The selection of appropriate sites

in arid regions can be challenging, as streams are ephemeral and fluvial transport may be sporadic (Nichols et al., 2002; Placzek et al., 2010; Mohren et al., 2020). Thus, there is a need to identify fluvial sediments sourced from, and thus representative of, the upstream area whose transport times are short relative to the decay of ^{10}Be . With these points in mind, catchments were chosen to conduct a sampling of the “active” channels. Before sampling, geological mapping of the catchments was initially carried out to assess lithological homogeneity and identify the primary source of the quartz target mineral in which ^{10}Be was measured. This mapping also aimed to identify the main sedimentological/erosional processes affecting the source rock. The selection of these catchments was based on four fundamental criteria: (a) the presence of downstream channels that partially or entirely erode the scarps; (b) the difference in catchment locations, selecting those situated both at the eastern boundary of the Cordillera de la Costa and in intramontane areas; (c) catchments located in our three study areas and (d) the likelihood of meeting the assumptions of the basin-averaging cosmogenic nuclide approach, such that the sediments reflect erosion of the upstream source area. The catchments were delineated via a 30-m resolution DEM (SRTM) obtained from <https://www.earthdata.nasa.gov>, and high-resolution DEMs were constructed using the SfM photogrammetry technique using Agisoft Metashape Professional, version 1.7.0.11701 (section 4.2).

4.3.2. Sampling strategy and processing

Sampling in the mouths of some catchments was avoided to mitigate the incorporation of sediments likely stored for significant periods in the prevalent alluvial fans. Instead, samples were collected further upstream closer to the headwaters of tributaries in each catchment, thereby characterizing erosion of the source rock. This strategy reduced the chance of potential contamination from previously exposed, fan-derived sediments while simultaneously minimizing sediment transport times. Owing to the limited quartz content in andesitic source rocks, the study focused on catchments exhibiting clear secondary mineralization signals and those with plutonic intrusions (ranging from diorite to quartz diorite). Catchments dominated by either andesite or intrusive were selected to ensure index mineral homogeneity. The secondary mineralization is characterized by recrystallized silica within amygdales and small veins. Bulk sediments were sampled in the field and later sieved (see supplementary material for details of sample preparation and measurement).

4.3.3. Erosion rate calculations

The LSDn scaling scheme (Lifton et al., 2014) was used to calculate the erosion rates via the online calculator of Balco et al. (2008) (<https://hess.ess.washington.edu>), assuming the mean elevation and coordinates of the basin. The online calculator is not explicitly intended for catchment-averaged erosion rate approaches, while complex catchment hypsometry could influence the production rate estimate. However, the catchments sampled are relatively small with low relief (Table S4) and so elevation biases on production rates are expected to be minimal. The input parameters used in the calculator are provided in the Supplementary Material (Table S5). Following the discussion in DiBiase (2018), the influence of topographic shielding on production rates was estimated as outlined in Binnie et al. (2006). To assess catchment erosion rates, we considered the individual subcatchment results. Interpretations for each catchment are based on the variability in subcatchment erosion rates, expressed as the range between minimum and maximum values. For catchments represented by a single measurement, that value was considered representative of the entire catchment.

4.4. Fault scarp deposits: pedogenic and mineralogical analyses

4.4.1. Pedogenic analysis

To investigate the role of salts in fault scarp preservation, the Naguayán and Salar del Carmen sites were selected as representative

study areas because of their well-preserved free faces. A pedogenic analysis of the deposits forming the original surfaces (prefaulting) was conducted to identify and describe the soil horizons, following the nomenclature established by Birkeland (1999). The soil horizons were delineated and characterized in the alluvial terraces through pedotrigraphic column representations, which included an evaluation of depth, protolith, structure, texture, and cementation.

4.4.2. Sedimentological description of fault scarp deposits

The fault scarp deposits were analysed via palaeoseismological trenches, providing a detailed sedimentary description. This analysis included: textural characteristics such as grain size, shape, and sorting; structural characteristics such as stratification and sedimentary structures; the degree and type of cementation; and postdepositional features.

4.4.3. Diffusion coefficient calculation

To estimate the rate of scarp degradation we measured the diffusion coefficient (k), which relates the area of the colluvial wedge formed by scarp degradation to the time elapsed since the most recent seismic event. The data used for this calculation were derived from trench mapping and the ages of colluvial wedges presented by González et al. (2025). The resulting diffusion coefficient is expressed in units of $\text{m}^2 \text{ ka}^{-1}$, providing a quantitative measure of the rate at which the scarp degrades due to diffusion processes.

4.4.4. X-ray diffraction (XRD) analysis

Samples from the soil horizons and fault scarp deposits were collected for X-ray diffraction (XRD) analysis to identify and semi-empirically define saline mineral phases.

Twenty-one representative samples were analysed by powder XRD at the Universidad Católica del Norte to determine their main mineral phases. The samples were homogenized by grinding with a mortar and pestle to obtain 10- μm -thick grains. XRD patterns were obtained using a Siemens D5000 diffractometer equipped with a 40-position sample holder, a coupled-theta goniometer, and a scintillation detector. A Siemens K 710H X-ray generator operating at a strength of 3 kW and a filament current of 40 mA was used. The diffraction patterns were recorded between 4° and 70° theta angles with a step size of 0.02° per second at room temperature. The patterns were evaluated semi-quantitatively via the TOPAS software package.

The samples used for XRD analysis excluded materials coarser than sand, such as debris or rock fragments, which were not considered soil constituents.

5. Results

5.1. Stratigraphy and sedimentary process

The regional stratigraphy is defined by three principal Cenozoic units: Miocene? –Pliocene gravels (U1), Pleistocene alluvial deposits (U2), and Late Pleistocene deposits (U3). These units are synthesized in a schematic chronostratigraphic diagram (Fig. 2).

(U1) Miocene? –Pliocene gravels: These conglomerates represent significant regional erosion and deposition events. Composed of strongly cemented, nonstratified and poorly stratified gravels, they are deposited along the western part of the Central Depression and within catchments of the Coastal Cordillera, reaching thicknesses of up to 100 m in Quebrada Mejillones (Cortés et al., 2007). They unconformably overlie the Mesozoic basement, are dissected by valleys and streams, and are covered by Late Pleistocene deposits. The gravels are clast-to matrix-supported, with strong gypsum cementation, and are interbedded with volcanic ash, as illustrated in the field photograph (Fig. 3c and e). Radiometric dating of volcanic ash layers sampled in this study yielded $^{40}\text{Ar}/^{39}\text{Ar}$ ages of 3.43 ± 0.02 Ma and 4.97 ± 0.02 Ma for sanidine in Quebrada Mititus and an age of 2.78 ± 0.02 Ma for biotite in Salar del Carmen (Table S12, Supplementary Material). Additional $^{40}\text{K}/^{40}\text{Ar}$ ages

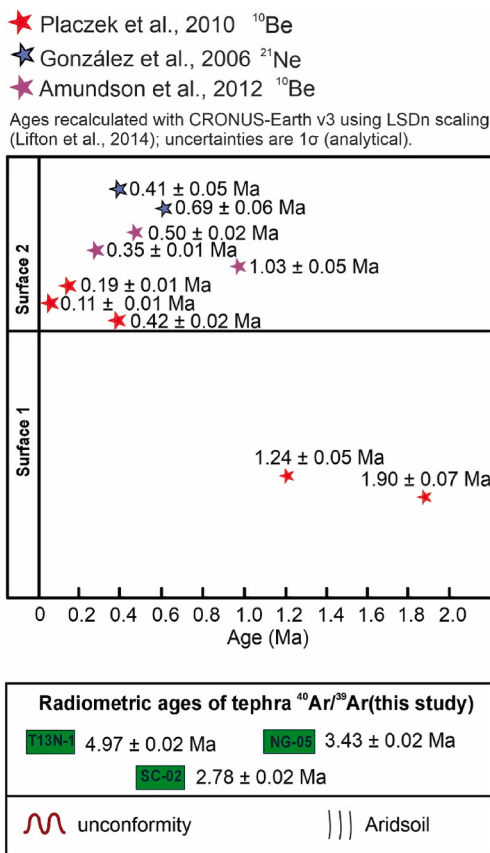


Fig. 2. Left: Diagram displays exposure ages reported in the literature for the area. Exposure ages shown diagram are as follows: (i) Amundson et al. (2012); ^{10}Be ; (ii) González et al. (2006); ^{21}Ne ; (iii) Placzek et al. (2010); ^{10}Be . All ages were recalculated with CRONUS-Earth v3 (Balco et al., 2008) using LSDn scaling (Lifton et al., 2014); uncertainties are internal. Right: Schematic chronostratigraphic diagram summarizing the regional stratigraphy, displaying the Cenozoic stratigraphic units: (U1) Miocene? -Pliocene gravels, (U2) Pleistocene alluvial deposits, and (U3) Late Pleistocene deposits. Tephra ages are reported at 2 σ ; all are $^{40}\text{Ar}/^{39}\text{Ar}$ total-fusion single-crystal laser-heating determinations; dated minerals: T13N-1, sanidine; SC-02, sanidine; NG-05, biotite. Figure edited in CorelDRAW Graphics Suite v.23.1.0.389, proprietary license.

of 3.0 ± 0.2 Ma and 5.2 ± 0.5 Ma for biotite were previously obtained in Salar del Carmen (Naranjo, 1987; González et al., 2003, respectively). The top of this unit is marked by a 1–2 m-thick gypsic soil crust. The cessation of U1 deposition is estimated to have occurred around the Early Pleistocene (ca. 1.24–1.90 Ma) on the basis of boulder exposure ages from the Coastal Cordillera (Placzek et al., 2010), although other studies (Amundson et al., 2012) suggest cessation at approximately 2.1 Ma.

(U2) Pleistocene alluvial deposits: These deposits form extensive alluvial fans predominantly at the piedmont of the Coastal Cordillera, overlying the Pliocene gravels. They consist of poorly sorted, clast-supported gravel with a sandy-granular matrix, are often interbedded with aeolian sandy layers and are characterized by variable gypsum cementation. The top of the deposit is marked by a 1 m-thick gypsic soil crust, designated Gs2 in this study, features clearly observed in the field outcrop shown in Fig. 3f. The cessation of U2 deposition at the Salar del Carmen piedmont is constrained by ^{21}Ne exposure ages of 686 ± 61 ka and 412 ± 46 ka (recalculated; see Methods; González et al., 2006). Additionally, published ^{10}Be surface-exposure ages from boulders near Quebrada Mititus (Placzek et al., 2010) are 424 ± 17 , 186 ± 7 , and 107 ± 5 ka (recalculated; see Methods).

(U3) Late Pleistocene deposits: These deposits occur at the foothills of the Coastal Cordillera, forming light grey alluvial fans with low slopes ($\sim 2^\circ$). They consist of loosely consolidated pebbles, sand, silt, and clay with minimal cementation as illustrated in Fig. 3a and b, which show typical sedimentary characteristics of U3 in the Salar del Carmen and Cerro Fortuna areas, respectively. Their distal facies are well developed

on plains, where they accumulate glaci in some areas. The deposits primarily originate from traction sediments mobilized by sporadic runoff, debris flows, and mudflows in valleys. These deposits are also present in ephemeral channels and fill in endorheic intermountain catchments, where they remain “active” due to evidence of debris flows. The Late Pleistocene unit (U3) includes deposits associated with the NGF scarp, dated at 21.4 ± 3.2 ka and 14.7 ± 1.0 ka (Del Río et al., 2019) and less extensive colluvial deposits from hillslope processes. Wind-blown sands and saline deposits also cover $\sim 8 \text{ km}^2$ near Salar del Carmen and are composed of silts, salt crusts, and halite.

5.2. Geomorphological surfaces

(S1) Surface 1: An aggradational surface that marks the end of the stratigraphic unit U1. Depositional features are lacking because of either well-developed desert pavement or the absence of desert pavement due to erosion, revealing the underlying soil. The distribution and geomorphic context of S1 are delineated in the geomorphological maps of the Naguayán, Cerro Fortuna, and Salar del Carmen areas (Figs. 4–6). Although channels have incised S1, the surface concurrently exhibits traits of smoothed relief. Upland bedrock erosion potentially culminated in the stripping of hillslope sediments and their deposition as widespread fan complexes at the end of the Pliocene (Jungers et al., 2013). The onset of preservation is constrained to the Early Pleistocene (1.24 ± 0.05 – 1.90 ± 0.07 Ma) by ^{10}Be surface-exposure ages for this surface, recalculated from Placzek et al. (2010) (see Methods).

(S2) Surface 2: The aggradational surface marks the end of

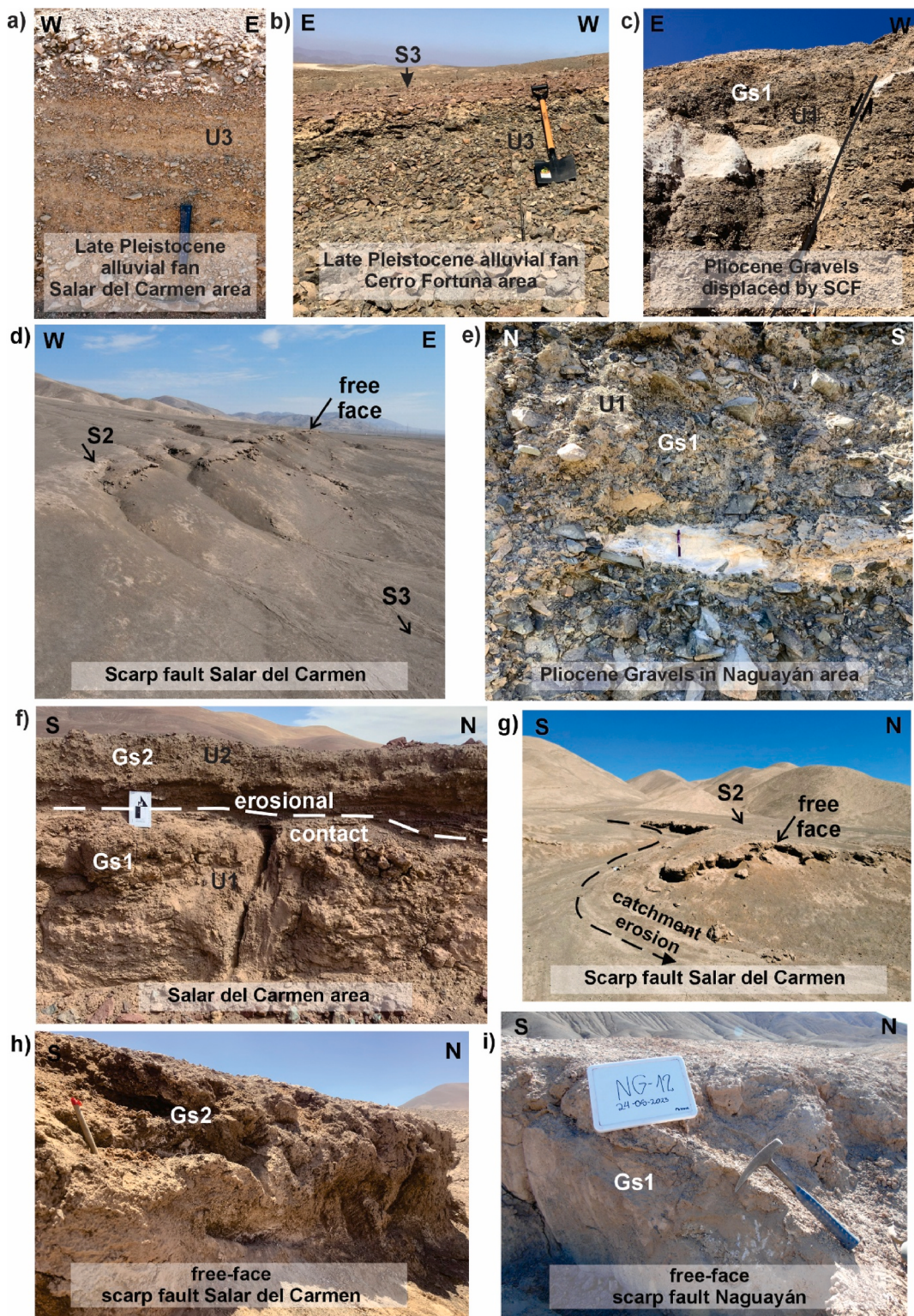


Fig. 3. (a) Photograph showing the deposits of stratigraphic unit U3 (Late Pleistocene) in Salar del Carmen. (b) Alluvial fan of unit U3 in the Cerro Fortuna area. (c) Ash lenses within Pliocene gravels of unit U1, displaced by the Salar del Carmen Fault. (d) Salar del Carmen fault scarp, highlighting the displaced S2 surface with distinct east-facing scarps and a well-developed free-face morphology. (e) Ash lenses within Pliocene gravels of unit U1 in the Naguayán area. (f) Erosional contacts between stratigraphic units U2 and U1, showing the development of gypsum soils Gs1 and Gs2 in Salar del Carmen. (g) Photograph of the Salar del Carmen fault scarp, emphasizing the presence of gypsum soil Gs2 and the erosion caused by main drainage channels. (h) Close-up view of the free-face in the Salar del Carmen fault scarp, illustrating the development of Gs2 in the stratigraphic unit U2. (i) Close-up view of the free-face in the Naguayán fault scarp, illustrating the development of Gs2 in the stratigraphic unit U2.

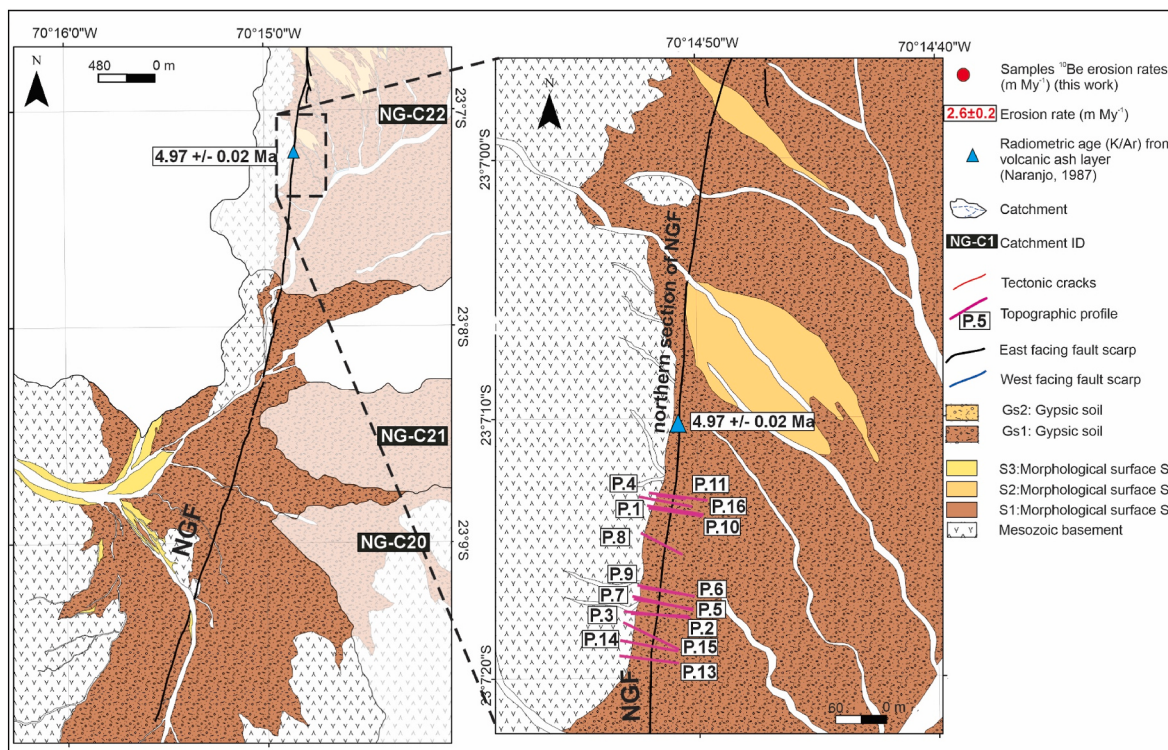


Fig. 4. Geomorphological map of the northern section of the Naguayán Fault (NGF), showing the geomorphological surfaces defined in this study (S1, S2) and the associated soils (Gs1 and Gs2). The blow-up map on the right displays the locations of the fault scarp profiles used for the morphometric analysis. Maps were produced using ArcMap 10.8.2 (Esri), proprietary license.

stratigraphic U2 and is distributed at the piedmont of the main mountain front of the eastern border of the Coastal Cordillera. Its spatial distribution is shown in the geomorphological maps provided in Figs. 4–6. It is composed of several large and coalescing alluvial fans of grey-dark colour caused by the development of desert varnish on clasts and the interlocking of clasts of desert pavement. In the Naguayán–Cerro Fortuna area, S2 presents a characteristic red colour. The slopes of this surface range between 5° and 7° for Naguayán and Cerro Fortuna and between 2° and 3° for Salar del Carmen. This surface is characterized by channel abandonment, stream capture, and the development of internal drainage, which predominantly incises into, or deposits onto, U3 towards the lower parts of the piedmont. These channels suggest that S2 has been modified by younger events, although in the field, they are commonly smooth features. Ephemeral pluvial episodes during the ongoing hyperarid climate (e.g., Ritter et al., 2019; Diederich et al., 2020) have incised the preexisting drainages on this surface. As fault displacement proceeds, these incisions are reactivated as feeder channels of the cone during short-lived rainfall events, producing a notched landscape. Preexisting drainages (gullies) near the scarp show an enhanced incision due to fault movement, with centimetre-scale knick-points being recorded.

5.3. Morphological characterization of fault scarps

The results indicate significant differences in the far-field slope between the Salar del Carmen region (4°) and the Naguayán area (10°). These data align with previous descriptions of the Coastal Cordillera piedmonts, as Hartley and Jolley (1995) reported. The values exhibit minimal variation relative to the mean, as demonstrated by the standard deviation versus mean slope graph (Fig. S1, Supplementary Material). Our study revealed that only two areas exhibit free faces, defined as angles between 40° and 90°. Specifically, Salar del Carmen and Naguayán have free faces with average slopes of 45° and 54°, respectively, as identified in the topographic profiles of each site (Fig. 7a).

Additionally, there is a marked difference in debris slope facies, with average inclinations of 33° in the scarp faults of Naguayán and 26° in Salar del Carmen. Cerro Fortuna shows a more advanced state of degradation than the other sites do, as it lacks a free face and primarily consists of debris slope facies, with an average angle of 26°. Further details on slope data, scarp metrics, and facies characterization are provided in the Supplementary Material (Tables S1 and S4).

In the SCF and NGF areas, there is a notable free face retreat of approximately 2 m, measured from the free face to the projection of the fault plane on the terrain surface. Applying the Wallace (1977) model of fault scarp degradation, 40 % of the profiles analysed in Naguayán and 54 % in Salar del Carmen are categorized as being in the gravity- and debris-controlled stage, which is the area where scarp faults have been most effectively preserved. The distribution of profiles among degradation stages is shown in Fig. 7b.

The results of the Ds index analysis for the southern section of the NGF, with a studied length of 6.1 km and fifteen analysis windows, displayed modal Ds values ranging from -0.8 to 1.0 (Fig. 8a). The northern section of the CFF, with a studied length of 6.8 km and fifteen analysis windows, presented modal Ds values ranging from -0.6 to 0.8 (Fig. 8b). For the SCF, the Manto de Varas segment, with a studied segment length of 6.1 km and fifteen analysis windows, yielded modal Ds values ranging from -0.9 to 1.0 (Fig. 9a). Los Morros segment, with a studied segment length of 3.1 km and ten analysis windows, produced modal Ds values between -0.9 and 1.0 (Fig. 9b) and similarly, Caracoles segment with a studied segment length of 3.3 km and nine analysis windows, yielded modal Ds values ranging from -0.9 to 1.0 (Fig. 9c).

5.4. Catchment morphology and erosion rates

The catchments of Naguayán area exhibit diverse morphologies, with some displaying an elongated shape that widens towards the headwaters, whereas others, such as NG-C3, have a palm-like form. These catchments have drainage areas ranging from 0.5 to 14 km² and a

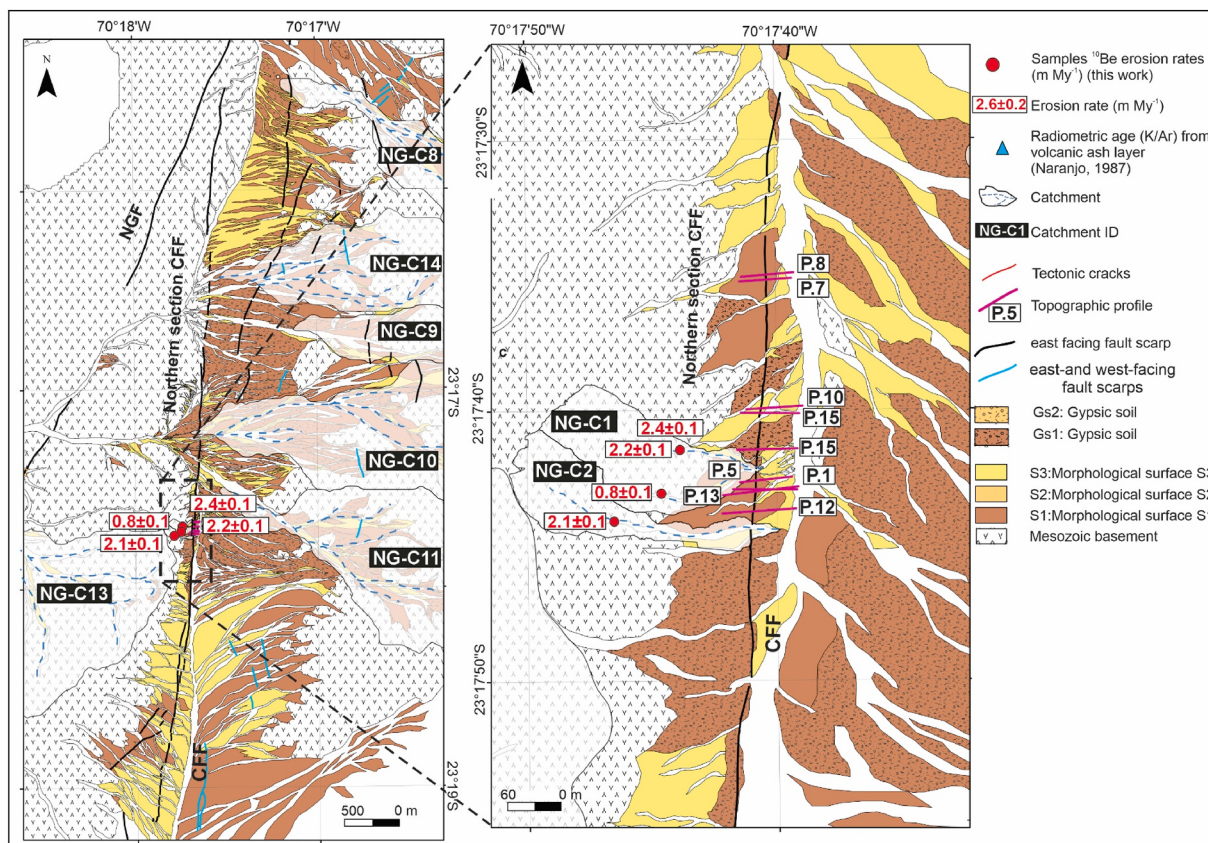


Fig. 5. Geomorphological map of the Cerro Fortuna (northern section), showing the geomorphological surfaces defined in this study (S1, S2) and the associated soils (Gs1 and Gs2). It also displays the catchments analysed in this study with their corresponding erosion-rate estimates. The blow-up map on the right displays the locations of the fault scarp profiles used for the morphometric analysis. Maps were produced using ArcMap 10.8.2 (Esri), proprietary license.

mean elevation between 713 and 1124 m a.s.l. The average slope of the catchments ranges from 13° to 27° . The predominant orientation is NW–SE, although in some areas, the catchments show an oblique alignment relative to the fault (Fig. 1). The main channel follows the long axis of the catchments, with its course oriented in a NW direction, whereas the tributaries display a dendritic pattern.

The catchments of the Salar del Carmen area exhibit an elongated morphology, with a mean elevation ranging from 703 to 1010 m a.s.l. The average slope of the catchments varies between 8° and 18° , and the drainage area ranges from 0.2 to 26 km 2 . The orientation of the long axis of the catchment is primarily NW–SE, with an oblique alignment relative to the fault, as shown in Fig. 1. The main channel follows the long axis of the catchments, with its course oriented in a SE direction, whereas the tributaries display a dendritic pattern. In some catchments, drainages exhibit knickpoints at locations where they coincide with fault segments. The youngest alluvial fans of stratigraphic unit U3, which are fed by these catchments, exhibit an isolated distribution and gentle slopes. Their apex is located at the base-level change, directly at the fault scarp, as shown in the geomorphological surface map of Fig. 6.

The catchments of Cerro Fortuna exhibit an elongated morphology, with mean elevations ranging between 780 and 1111 km and drainage areas between 0.01 and 2.2 km 2 . The average slope of the catchments ranges from 13° to 28° . Their predominant orientation is E–W, which is perpendicular to the fault, as shown in Fig. 1. The main channels follow the long axis of the catchments, with their flow direction varying between catchments. The NG-14, NG-9, NG-10, and NG-11 catchments, which drain westwards, have an average drainage area of 2 km 2 , whereas the NG-C1 and NG-C2 subcatchments, which drain eastwards, have significantly smaller drainage areas, averaging only a few dozen square metres. The tributaries of the W-draining catchments display a

dendritic pattern, whereas the E-draining catchments are characterized by straight channels.

The blank-corrected concentrations of ^{10}Be in 17 samples ranged from $1.43 \pm 0.06 (\times 10^6)$ atoms/g to $2.60 \pm 0.10 (\times 10^6)$ atoms/g. The maximum blank corrections were less than 13 % of the total ^{10}Be measured. On the basis of these concentrations, the erosion rates per sample vary between 0.51 and 2.86 m Ma $^{-1}$ (Table 1). In Salar del Carmen, the catchment SC-C4 is represented by a single erosion rate of 2.62 ± 0.09 m Ma $^{-1}$. In catchment SC-C5, erosion rates range from 0.51 ± 0.04 to 1.40 ± 0.09 m Ma $^{-1}$, whereas in catchment SC-C6 the erosion rate is 1.10 ± 0.05 m Ma $^{-1}$. In Naguayán, erosion rates in catchment NG-C3 range from 1.41 ± 0.07 to 2.15 ± 0.10 m Ma $^{-1}$, and from 2.36 ± 0.11 to 2.86 ± 0.12 m Ma $^{-1}$ in catchment NG-C4. In Cerro Fortuna, catchment NG-C1 shows erosion rates between 0.76 ± 0.04 and 2.38 ± 0.13 m Ma $^{-1}$, while NG-C2 is represented by a single value of 2.05 ± 0.12 m Ma $^{-1}$. The highest rate was observed in NG-C4, whereas the lowest is in SC-C5 (Table 1).

5.5. Soil profile characterization and sulfate salt Quantification

On the basis of the pedogenic analyses conducted on prefault deposits, two significant soil horizons were identified, referred to in this study as Gs1 and Gs2. Gs1 developed in the deposits of stratigraphic unit U1, whereas Gs2 formed in the deposits of stratigraphic unit U2.

The pedostratigraphic columns, described following the nomenclature of Birkeland (1999), reveal that the By horizon of Gs1 is approximately 1 m thick and displays a Munsell colour of 10YR6/2. The By horizon Gs1 is characterized by a massive structure, with angular to subangular clasts embedded within a sulfated matrix, columnar block textures, and cementation classified as indurated. In the Naguayán area,

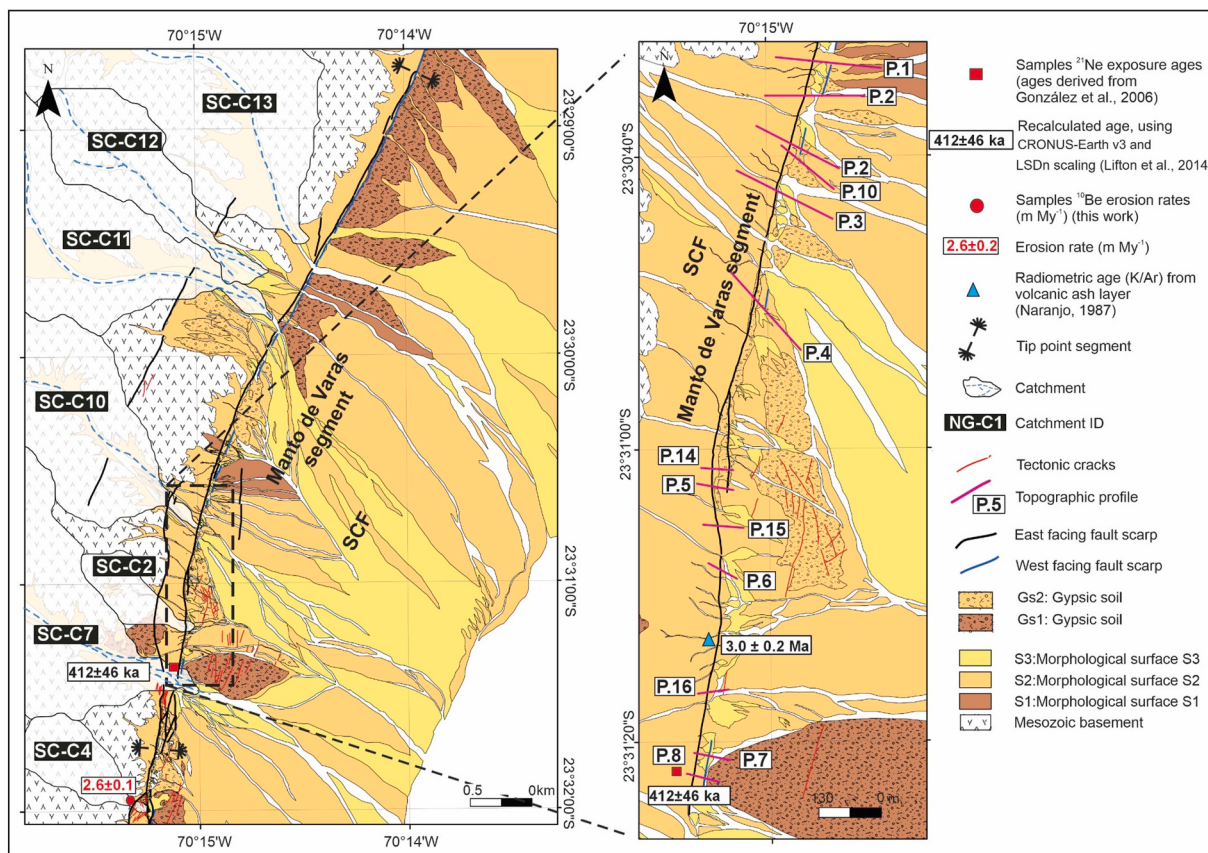


Fig. 6. Geomorphological map of the Salar del Carmen Fault (Manto de Varas segment), showing the geomorphological surfaces defined in this study (S1, S2) and the associated soils (Gs1 and Gs2). The map shows exposure-age samples from previous studies, recalculated with CRONUS-Earth v3 (Balco et al., 2008) using LSDn scaling (Lifton et al., 2014); uncertainties are internal. It also displays the catchments analysed in this study with their corresponding erosion-rate estimates. The blow-up map on the right displays the locations of the fault scarp profiles used for the morphometric analysis. Maps were produced using ArcMap 10.8.2 (Esri), proprietary license.

this soil contains gypsum crystals within its matrix. Field evidence indicates that Gs1 is displaced by reverse faulting, which is subsequently cut by later normal faulting, resulting in east-facing scarps observed at both the Naguayán and Salar del Carmen sites, as illustrated in the schematic diagrams of Figs. 10 and 11, respectively.

The By horizon Gs2 is approximately 60–80 cm thick and presents a Munsell colour of 10YR7/3. While it retains some sedimentary features of the protolith, such as the original stratification of the alluvial deposit, it has a single-grain structure, with angular to subangular clasts embedded within a sulfated matrix, granular texture, and moderate cementation. Field evidence indicates that Gs2 is displaced by normal faulting, as observed at the Naguayán and Salar del Carmen sites (Figs. 10 and 11, respectively).

According to the classification proposed by González et al. (2025), the deposits associated with scarp degradation can be grouped into two main categories: colluvial wedges and wash deposits. The tectonic origin of the colluvial wedges was determined by these authors through the identification of event horizons and faults sealed by successively stacked colluvial wedges, in which younger units systematically overlie older ones. At Naguayán, two colluvial units with irregular morphology but continuity along the slope were identified, referred to here as Cw1 and Cw2 in the schematic diagram shown in Fig. 10. Units Cw1 and Cw2 are both composed of well-sorted, pebble-sized, angular clasts embedded in a clay matrix and weakly cemented by sulfate salts. A total thickness of 1.0 ± 0.05 m for the Cw1 wedge was previously measured in this trench by González et al. (2025). Wash deposits are observed from the mid-scarp to the base. These deposits are well sorted, are predominantly composed of a clay matrix, are weakly cemented by sulfate salts, and

exhibit stratification.

The schematic scarp profile of the SCF (Fig. 11) illustrates three colluvial units: Cw1, Cw2, and Cw3, which display regular and continuous morphologies along the slope. Cw1, contains poorly sorted, pebble-sized, subangular clasts embedded in a silty-clay matrix and is moderately cemented by sulfate salts. Cw2, is characterized by well-sorted, pebble-sized, subangular clasts, which are primarily clast-supported and weakly cemented by sulfate salts. Cw3, is also well-sorted, clast-supported, and weakly cemented. According to González et al. (2025), Cw1, Cw2, and Cw3 reach thicknesses of 0.8 ± 0.05 m, 1.0 ± 0.05 m, and 1.2 ± 0.05 m, respectively. Wash deposits were observed in Cw2 and Cw3, where stratification and very thin interbedded silt–clay layers alternating with clast-supported layers become more pronounced farther from the fault plane, with wedge structures commonly developed within these deposits.

We determined the diffusion coefficient (k) for the scarp at Salar del Carmen by calculating the ratio between the area of the colluvial wedge Cw3 (3.4 m^2) and the modelled age of the most recent earthquake—estimated at 59 ± 17 ka by Gonzalez et al. (2025)—yielding a value of $k = 0.063 \pm 0.018 \text{ m}^2 \text{ ka}^{-1}$.

XRD analyses of the soil horizon Gs1 at Salar del Carmen revealed an average composition of 41 % anhydrite, 34 % gypsum, and 0.2 % bassanite. In contrast, Gs1 at Naguayán presented an average of 33 % anhydrite and 21 % gypsum, with no bassanite detected. The samples from the free face of Salar del Carmen developed within the soil horizon Gs2 contained an average of 28 % gypsum and 10 % anhydrite. In contrast, the free face at Naguayán developed within the soil horizon Gs1 contained 76 % gypsum with no other sulfate species detected

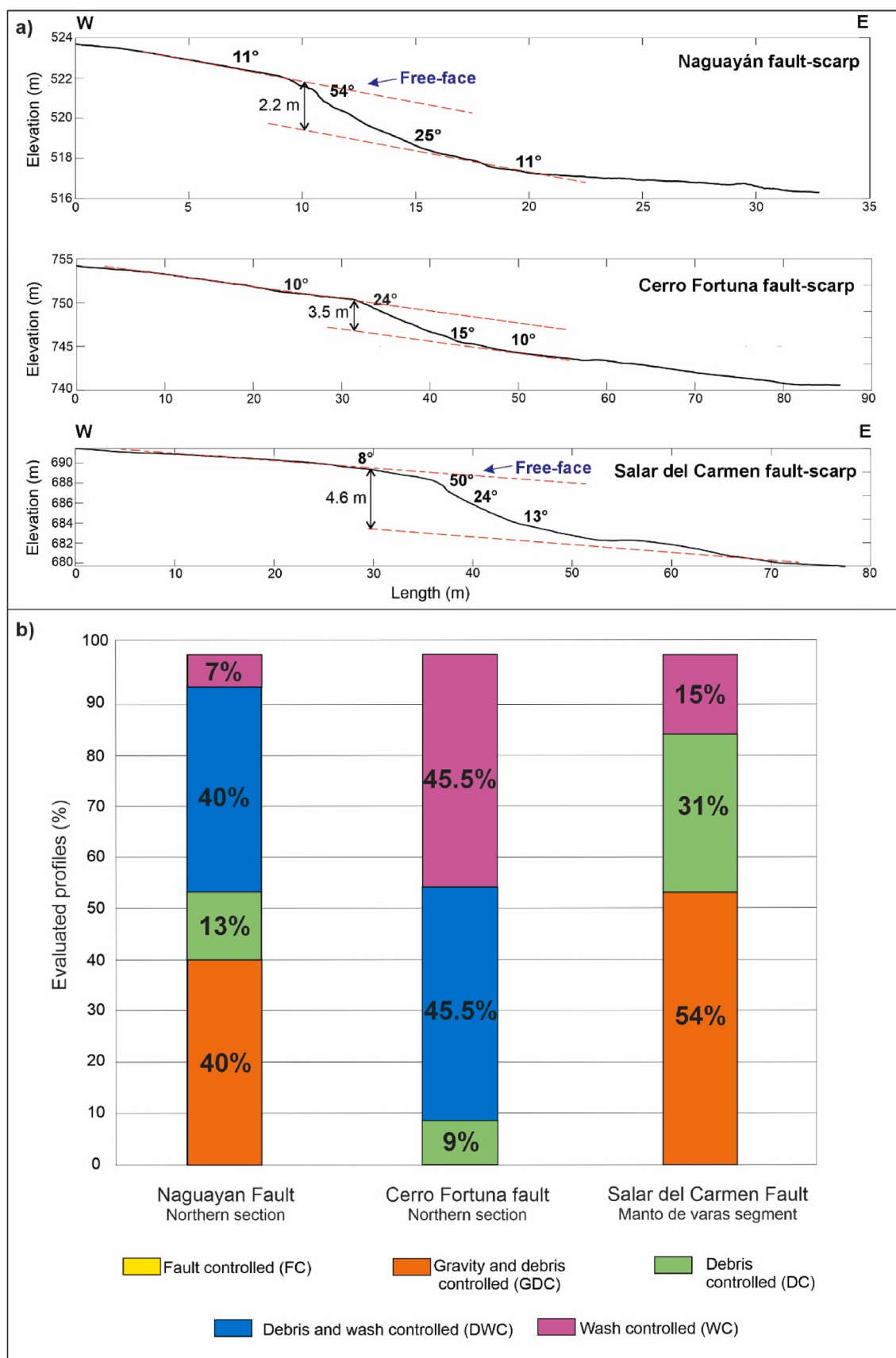


Fig. 7. a) Topographic profiles of fault scarps in the three study areas. Note the presence of free faces in the Naguayán and Salar del Carmen regions. b) Graph that provides the percentage of the profile corresponding to every stage of degradation (Wallace, 1977). These data were separated by fault. CFN: Cerro Fortuna, NGN: Naguayán and SCF: Salar del Carmen. Figure edited in CorelDRAW Graphics Suite v.23.1.0.389, proprietary license.

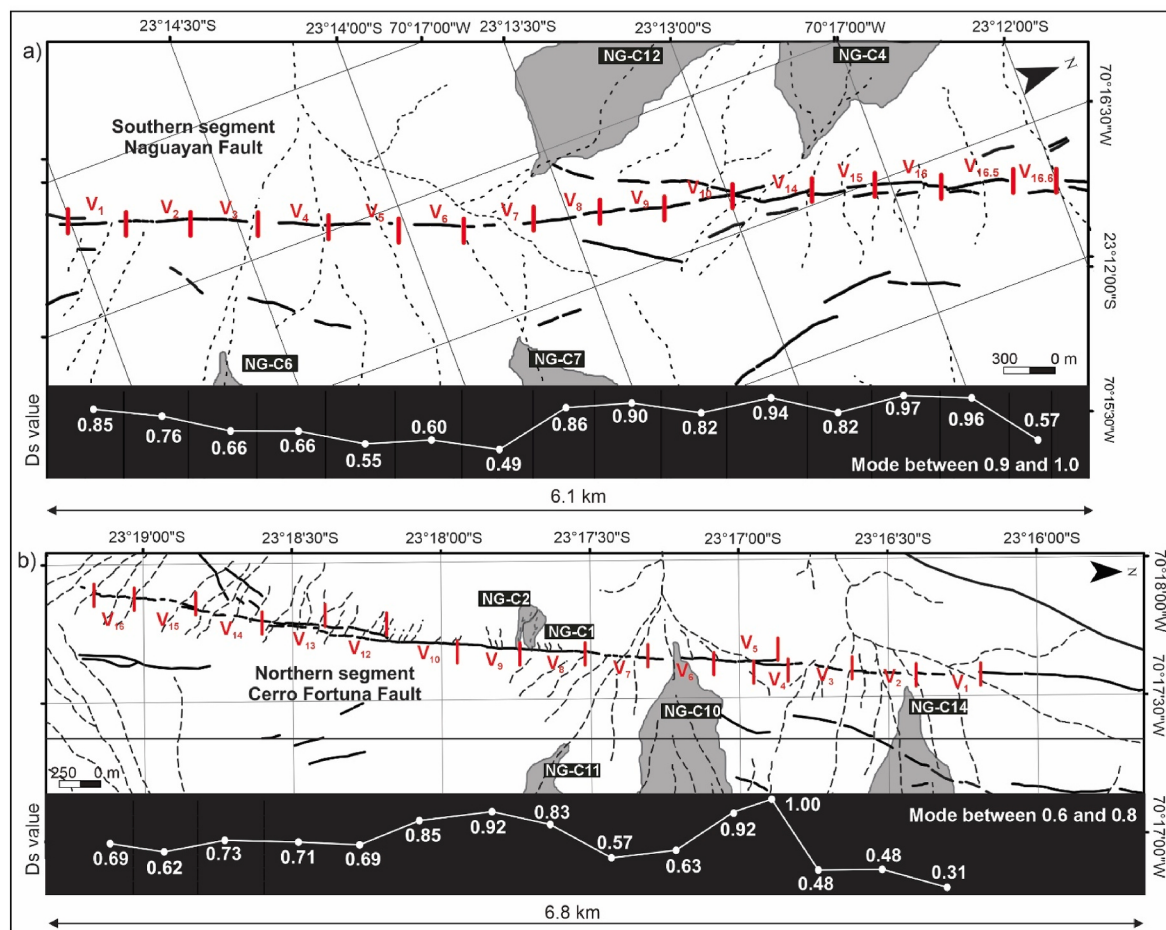


Fig. 8. Surface fault trace maps used for the analysis of the morphometric index Ds. a) Naguayán Fault (southern section). b) Cerro Fortuna Fault (northern section). Red lines indicate the analysis windows, each 400 m in length. Grey polygons represent coastal cordillera catchments draining towards the fault scarps. Below each surface fault trace, the Ds values for each analysis window are shown. A Ds value of 1 indicates a dominance of tectonic uplift over erosional processes, while a Ds value of 0 reflects a significant impact of catchment erosion on scarp faults. For the formula used to calculate the Ds index, refer to the main text. Maps were produced using ArcMap 10.8.2 (Esri), proprietary license.

(Fig. 12, bar diagram showing gypsum and anhydrite content in paleos Gs1 and Gs2).

For the fault scarp deposits at Salar del Carmen, the XRD results revealed that Cw1 contains 18 % gypsum and 4 % anhydrite, Cw2 contains 3.6 % gypsum, and Cw3 contains 5.2 % gypsum. In contrast, the wash deposits at this site contained an average of 1.0 % gypsum and 0.1 % anhydrite. Similarly, XRD analyses of wash deposits from the fault scarp at Naguayán revealed 1.2 % anhydrite and 0.5 % gypsum (Fig. 12, bar diagram showing gypsum and anhydrite content in scarp deposits).

The pseudoternary diagrams in Fig. 12 illustrate notable variability in the relative proportions of gypsum and anhydrite across the different sample groups (Gs1, Gs2, and scarp deposits). While some samples are dominated by gypsum, others exhibit a predominance of anhydrite, highlighting the heterogeneity in sulfate mineral assemblages.

6. Discussion

One of the most critical aspects of this work is to explain how extremely old fault scarps preserve a free face and why the prevailing Late Quaternary denudation was not able to remove fault-related morphologies (free face and colluvial wedges) that formed tens of thousands of years ago. A simple answer to this question is the ability of hyperaridity in the Atacama Desert since the Late Pleistocene (Amundson et al., 2012) to preserve topography. However, details of the driving factors are not included in this answer, and they are important for

elucidating how climate and its interactions with surface geomorphic processes control fault scarp degradation. In particular, the dependence of colluvial wedge formation on climate conditions has been formulated only in a general way. There is a substantial gap in the determination of the circumstances under which colluvial wedges are formed and preserved (Gray et al., 2022). Because colluvial wedges are fed from the erosion of the free face, at least in the early stages of scarp degradation, a comprehensive understanding of colluvial wedge facies is strongly relevant for this purpose.

6.1. Free face preservation and colluvial wedge formation

Free face preservation and colluvial wedge formation in the Atacama Desert are dependent on the following driving factors: (1) Fault scarps in the study area degrade through slow diffusive processes interspersed by very localized channel incisions associated with catchment reactivation during rare rainfall events, and (2) pedogenetic processes leading to salt impregnation in faulted alluvial deposits exerts cementing effects that prevent the collapse of the free face.

According to the slope analysis, the fault scarps in our study are predominantly characterized by debris slopes, with localized sections (e.g., the Salar del Carmen and Naguayán Faults) exhibiting retreating free faces. This limited degradation underscores the critical role of extreme aridity, which drives key processes such as (1) daily temperature fluctuations, (2) salt dissolution facilitated by fog moisture, and (3) pore-

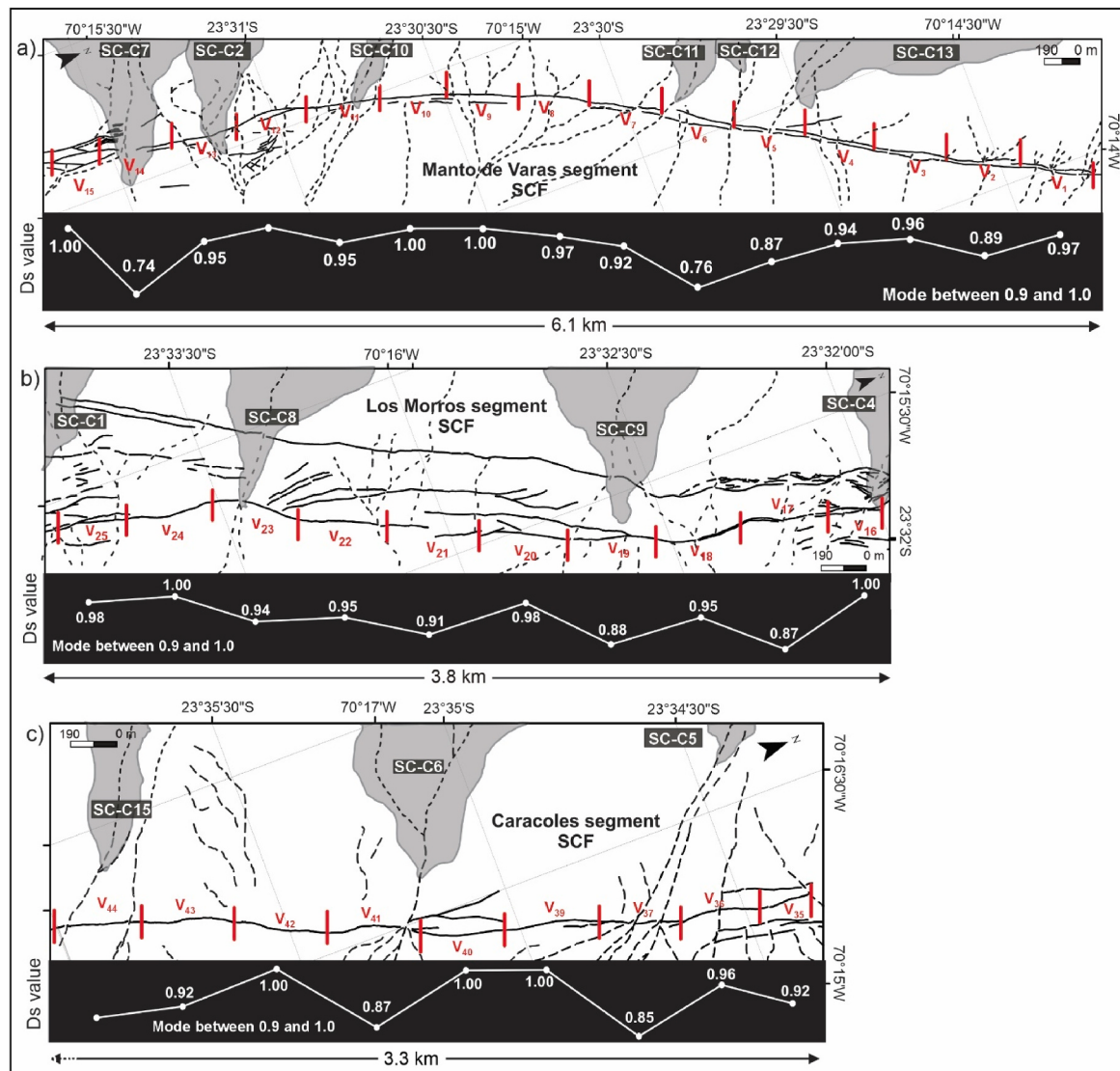


Fig. 9. Surface fault trace maps used for the analysis of the morphometric index Ds. (a) Salar del Carmen Fault: Manto de Varas segment; (b) Los Morros segment; and (c) Caracoles segment. Red lines indicate the analysis windows, each 400 m in length. Grey polygons represent coastal cordillera catchments draining toward the fault scarps. Below each segment, the corresponding Ds values for each analysis window are shown. A Ds value of 1 indicates a dominance of tectonic uplift over erosional processes, whereas a value of 0 reflects a significant impact of catchment erosion on fault scarp morphology. For the formula used to calculate the Ds index, refer to the main text. Maps were produced using ArcMap 10.8.2 (Esri), proprietary license.

water evaporation. These processes gradually release clasts from stratigraphic units U1 and U2. The mobilized clasts move downslope through gravity-driven processes, contributing to debris formation. The onlapping debris layers consist of well-laminated, clast-supported deposits interbedded with microhorizons of soils. Over time, older colluvial deposits have indurated, with shattered clasts and sulfate salts in their fine fraction, indicating an incipient pedogenic process in postfaulting colluvium.

The diffusion coefficient calculated for the fault scarp at Salar del Carmen yielded a value of $k = 0.063 \pm 0.018 \text{ m}^2 \text{ ka}^{-1}$. In contrast, significantly higher diffusion coefficients have been reported in other areas of the world; for example, Nash (1980) reported $k = 0.46 \text{ m}^2 \text{ ka}^{-1}$ in the basin and range region, whereas values in Negev, Israel, range from 0.1 to $0.4 \text{ m}^2 \text{ ka}^{-1}$ (Begin, 1992; Enzel et al., 1996). These variations in k express the sensitivity of the diffusion constant to variations in material properties and local climatic conditions. Consequently, our measured value represents one of the lowest diffusion coefficients reported globally, which is consistent with the hyperarid conditions of northern Chile.

Wash elements in colluvial wedges indicate secondary redistribution of debris, where material initially removed from the scarp has been further reworked by sporadic runoff and rain splash, reflecting a gradual transition in sediment distribution over extended transport times. The evidence supporting this interpretation is the lateral contact between the debris and wash facies (González et al., 2025). The occurrence of stratified sandy gravels with silt intercalations and incipient cementation by reprecipitated salts, together with interbedded, well-sorted, fine-to medium-grained aeolian sand lenses displaying parallel to horizontal lamination (Del Río et al., 2019), indicates episodic alternation between colluvial deposition and aeolian sediment input. In this context, aeolian activity contributed mainly as a sediment source, while wind erosion is minimal due to salt-induced cementation of the scarp deposits.

Our results indicate that the scarps show no evidence of progressive crest rounding or significant basal concavity. The free faces, maintaining angles between 45° and 54° , have retreated approximately 2 m since the last faulting event ($59 \pm 17 \text{ ka}$; González et al., 2025) in Salar del Carmen. For this area, we estimate a retreat rate of $\sim 0.03 \text{ m ky}^{-1}$. Preservation of these free faces is linked to prefaulting gypsum soils (By) with

Table 1

Variables used to derive catchment-average erosion rate.

Table 1: Summary of cosmogenic nuclide data, assuming a density of 2.7 g/cm^3 and applying a thickness of 0.025 cm in the online calculator, corresponding to the maximum grain size sampled. Latitude and longitude correspond to the centroid of the catchment. All calculations were performed using the 07KNSTD std in the input of the CRONUS-Earth v3. LSDn scaling scheme (Lifton et al., 2014) was used to derive production rates. All errors are σ (uncertainties are 1σ analytical). See supplementary data for more details and inputs.

Sample ID	Catchment ID	Latitude ($^{\circ}$)	Longitude ($^{\circ}$)	Elevation (m.a.s.l)	Scaling factor	^{10}Be concentration (atoms/g)	^{10}Be erosion rate (m Myr $^{-1}$)	Int. Unc. (m Myr $^{-1}$)
NG-C1-03	NG-C1	-23.2949	-70.2959	788	0.9919	$1.27 \times 10^6 \pm 0.06 \times 10^6$	2.38	0.13
NG-C1-03 II						$1.36 \times 10^6 \pm 0.07 \times 10^6$	2.20	0.14
NG-C1-04A						$3.20 \times 10^6 \pm 0.12 \times 10^6$	0.76	0.04
NG-C2-02	NG-C2	-23.2953	-70.2959	781	0.9950	$1.46 \times 10^6 \pm 0.08 \times 10^6$	2.05	0.12
NG-C3-04	NG-C3	-23.2484	-70.2397	1124	0.9985	$2.10 \times 10^6 \pm 0.13 \times 10^6$	1.81	0.13
NG-C3-05						$2.53 \times 10^6 \pm 0.10 \times 10^6$	1.45	0.07
NG-C3-06						$2.03 \times 10^6 \pm 0.10 \times 10^6$	1.88	0.10
NG-C3-07						$1.81 \times 10^6 \pm 0.07 \times 10^6$	2.15	0.10
NG-C3-08						$2.60 \times 10^6 \pm 0.10 \times 10^6$	1.41	0.07
NG-C4-01	NG-C4	-23.2077	-70.2819	925	0.9967	$1.43 \times 10^6 \pm 0.06 \times 10^6$	2.36	0.11
NG-C4-02						$1.21 \times 10^6 \pm 0.05 \times 10^6$	2.86	0.12
NG-C4-03						$1.38 \times 10^6 \pm 0.07 \times 10^6$	2.46	0.13
SC-C4-01	SC-C4	-23.5295	-70.2601	780	0.9987	$1.31 \times 10^6 \pm 0.04 \times 10^6$	2.62	0.09
SC-C5-03	SC-C5	-23.5585	-70.3064	895	0.9999	$4.24 \times 10^6 \pm 0.15 \times 10^6$	0.59	0.03
SC-C5-05A						$4.66 \times 10^6 \pm 0.23 \times 10^6$	0.51	0.04
SC-C5-06						$2.19 \times 10^6 \pm 0.12 \times 10^6$	1.40	0.09
SC-C6-01	SC-C6	-23.6000	-70.2910	790	0.9967	$2.31 \times 10^6 \pm 0.08 \times 10^6$	1.10	0.05

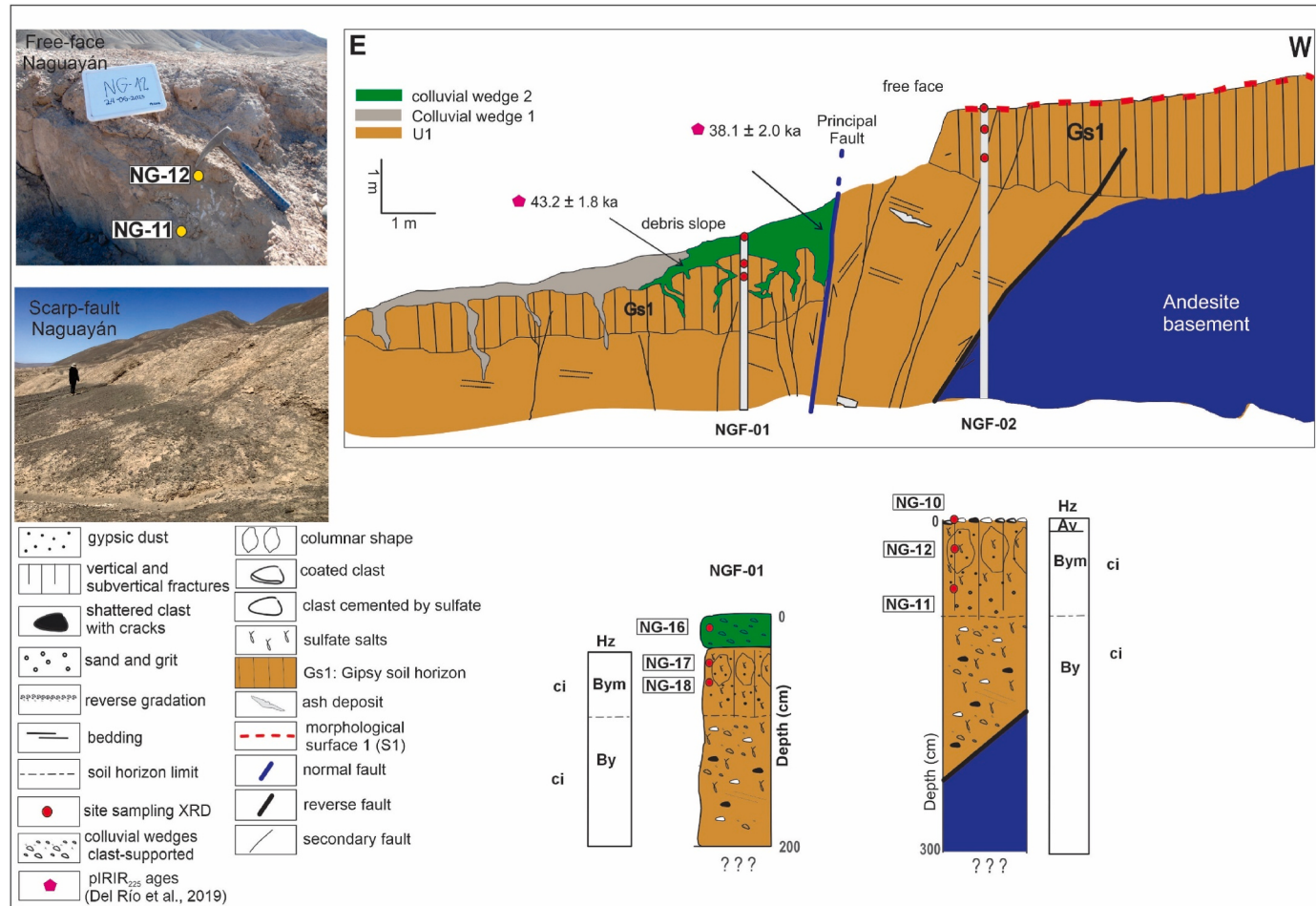


Fig. 10. Schematic diagram of the Naguayán Fault scarp, showing pedo-stratigraphic columns NGF-01 and NGF-02. Soil horizon nomenclature follows Birkeland (1999). Detailed descriptions of the soil profiles are provided in Table S9 of the Supplementary Material. Sedimentological data for associated scarp-derived deposits are available in Table S11. Colluvial wedges, originally identified and described by González et al. (2025), are represented schematically. Red circles indicate the locations of samples analysed by XRD. Figure edited in CorelDRAW Graphics Suite v.23.1.0.389, proprietary license.

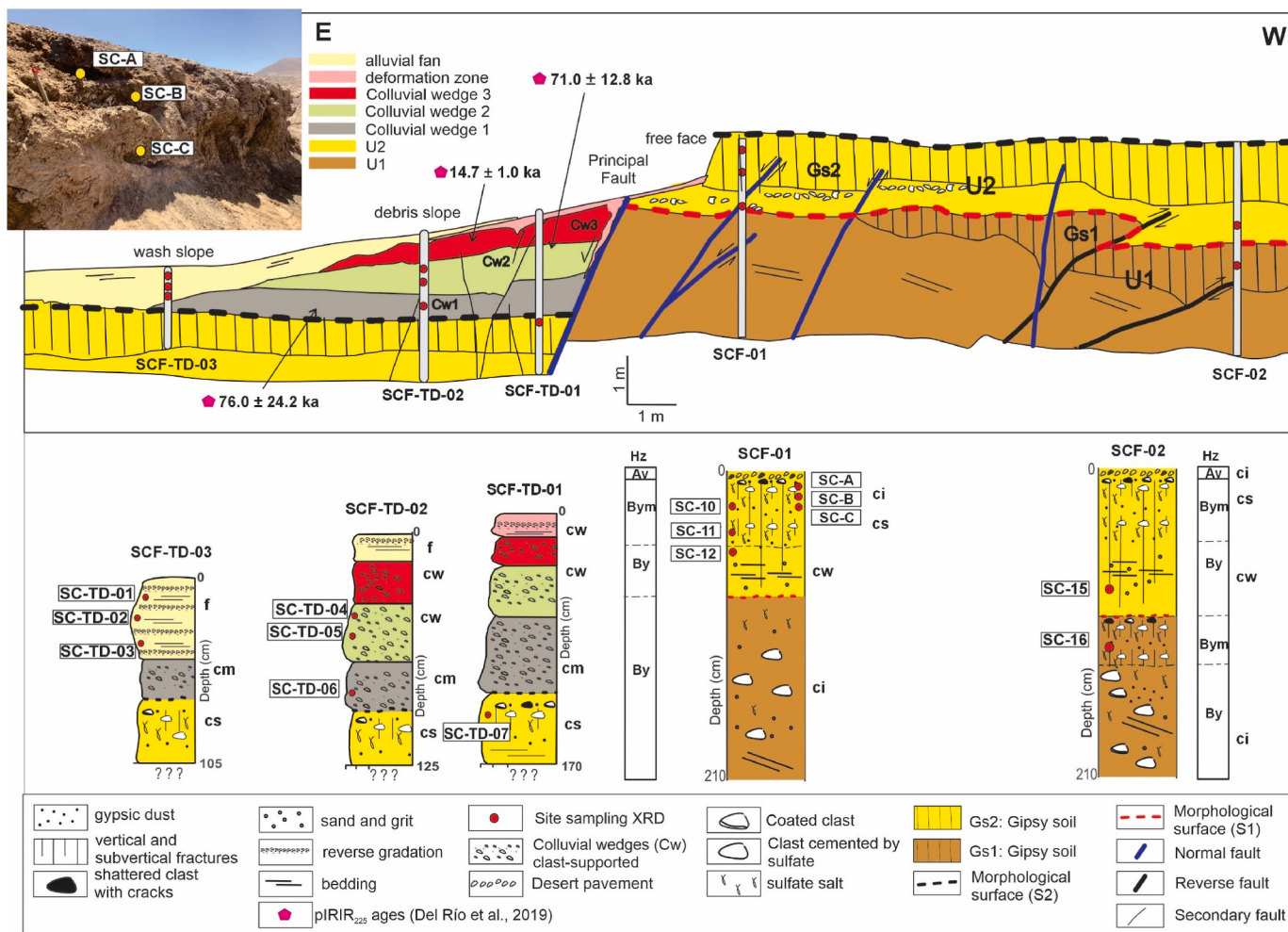


Fig. 11. Schematic diagram of Salar del Carmen fault scarp, showing pedo-stratigraphic columns SCF-01 and SCF-02, with soil horizon nomenclature following Birkeland (1999). Detailed descriptions of the soil profiles are available in Tables S7 and S8 of the Supplementary Material. Sedimentological columns SCF-TD-01, SCF-TD-02, and SCF-TD-03 depict the compositional and textural characteristics of deposits resulting from scarp degradation. Colluvial wedges, originally identified and described by González et al. (2025), are represented schematically. Additional sedimentological data for these scarp-derived deposits are provided in Table S10 of the Supplementary Material. Red circles indicate the locations of samples analysed by XRD. Figure edited in CorelDRAW Graphics Suite v.23.1.0.389, proprietary license.

high sulfate concentrations, identified as Gs1 and Gs2. The predominance of gypsum near the surface suggests that it is the most stable phase under the current hyperarid conditions of the region, likely maintained by minimal but recurrent moisture inputs from fog (*camanchaca*). The higher proportions of anhydrite in Gs1 may reflect the slow transformation of gypsum to anhydrite over geological timescales (Voigt et al., 2020). These soils enhance induration through clast cementation, increasing resistance to erosion and limiting the lateral collapse rate of the free face.

The global distribution of fault scarps across diverse geographic and climatic settings indicates that free faces may persist for decades to several hundred years (Kogan and Bendick, 2011). Their presence is a geomorphic marker of historical seismicity (e.g., Wallace, 1977; Caskey et al., 1996; Buchun et al., 1986; Hanks and Schwartz, 1987). In stark contrast, our findings reveal that surface deformation features persist for tens of thousands of years in the hyperarid Atacama Desert. This extraordinary long-term preservation occurs when average landscape erosion rates are on the order of a few metres per million years or less and represents an apparent anomaly relative to expected degradation rates in other climatic contexts, challenging existing models of scarp evolution. Moreover, this result hints at the extremely low background erosion rates required for fault scarps to reflect much older activity; in the absence of direct dating methods, background erosion rates in arid

environments could serve as a proxy to estimate the potential survival time of preserved scarps, thereby refining predictions of fault activity.

6.2. Along-strike degradation of fault scarps

According to the morphometric index (Ds) results, SCF and NGF have values ranging between 0.9 and 1.0, indicating minimal along-strike fault scarp degradation resulting from channel erosion. These findings are consistent with the generally low erosion rates obtained for catchments in the Coastal Cordillera (0.5–2.9 m Ma⁻¹; Table 1). In contrast, a difference in Ds values was observed in the CFF, ranging between 0.6 and 0.8. This can be attributed to the steeper piedmont, characterized by catchment slopes ranging from 16° to 19°, which enhances stream power, thereby promoting the degradation of abandoned surfaces S1 and S2 and the deposition of alluvial fans associated with stratigraphic unit U3, forming the surface referred to in this study as S3.

These geomorphic contrasts indicate that scarp preservation depends not only on local topographic settings but also on longer-term tectonic and climatic controls. According to González et al. (2025), the scarps of the AFS are rejuvenated by seismic events; during this process, the catchments gradually recover an equilibrium channel profile. This suggests that rainfall events capable of driving fluvial processes are rare but likely of high intensity, leading to significant erosion, or burial, that can

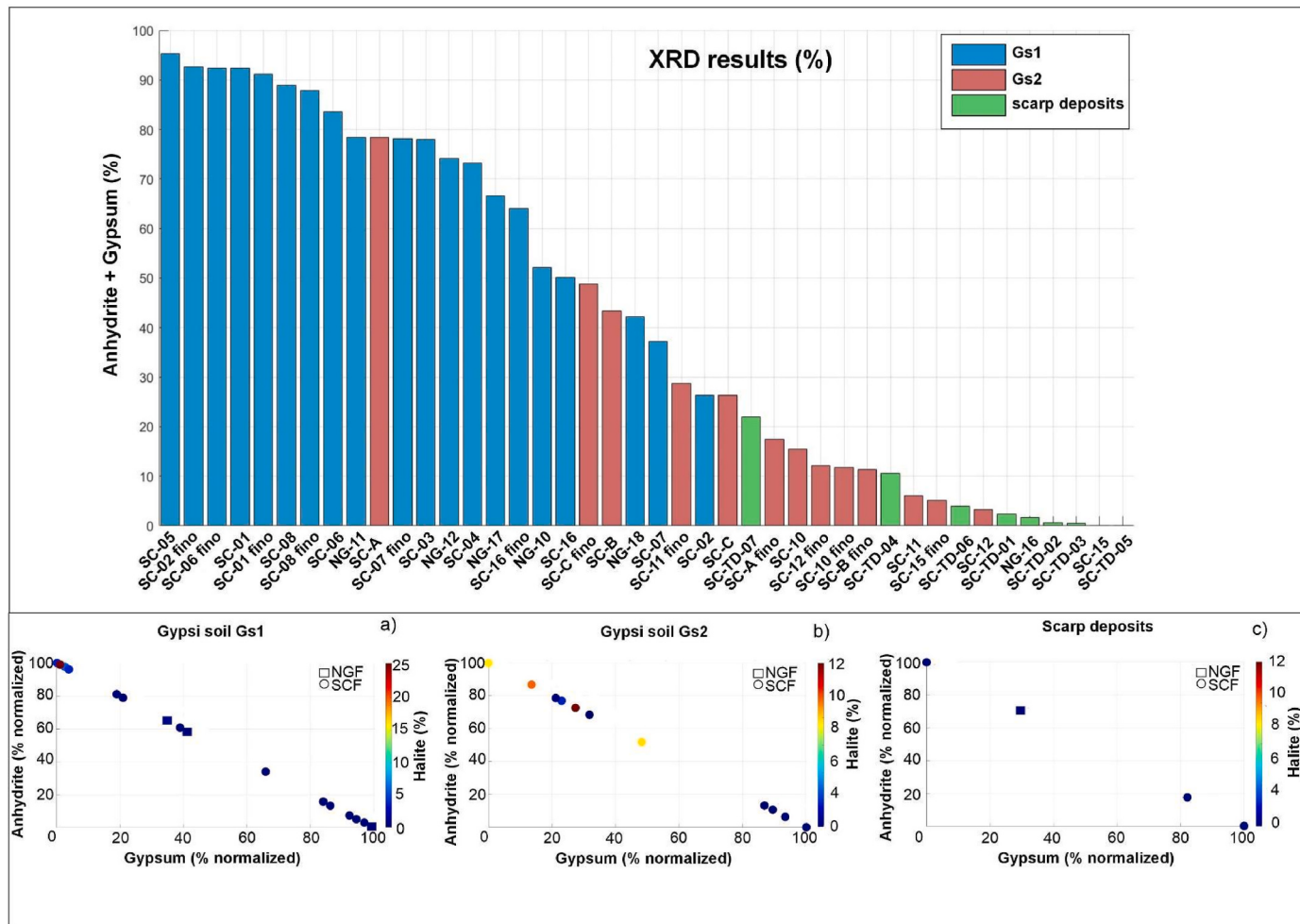


Fig. 12. Top: Bar diagram showing the abundance of sulfate salts (anhydrite + gypsum) derived from XRD analysis. Samples were collected from gypsiferous soil horizons Gs1 (blue), Gs2 (red), and from scarp deposits (green). The stratigraphic position of representative samples is illustrated in the pedo-stratigraphic profiles in Fig. 10 and 11. Bottom: Pseudoternary diagrams showing the normalized contents of gypsum (x-axis) and anhydrite (y-axis) for samples from (a) Gs1, (b) Gs2, and (c) scarp deposits. Normalized values correspond to the relative proportions of gypsum and anhydrite within each sample. For normalization, the percentages of both minerals were summed and set to 100 %, and the contribution of each mineral was then recalculated as a percentage of this total. The color scale to the right represents halite abundance, with cooler colors indicating relatively lower values and warmer colors indicating relatively higher values within each group. Note that halite abundance is shown on different scales for each group. Graphs were generated using MATLAB R2023b, proprietary license.

erases portions of the scarp record in areas where channels intersect it. However, this erosion process is insufficient to completely degrade the scarp or compensate for the slow slip rate of the NGF and SCF, estimated at approximately 0.07 mm yr^{-1} (González et al., 2025). Consequently, the fault scarps remain well preserved, reflecting a prolonged long-term geomorphic response to sustained but slow tectonic activity.

6.3. Limitations of cosmogenic erosion rate estimates in hyperarid environments

The variation in erosion rates between subcatchments that are in close proximity is higher than might be expected, with ~3-fold differences observed in catchments NG-C1 (0.76 ± 0.04 to $2.38 \pm 0.13 \text{ m Ma}^{-1}$) and SC-C5 (0.51 ± 0.04 to $1.40 \pm 0.09 \text{ m Ma}^{-1}$). While we assume the variation in rates to reflect variable erosion of the source areas, we cannot discount the potential for biases in such a low energy setting, where assumptions inherent to the basin-wide approach become strained. In particular, the criteria for relatively rapid transport of eroded sediments to, and through, fluvial systems (Bierman and Steig, 1996) may not be met, resulting in ^{10}Be signals which may be too low due to ^{10}Be decay during long-term storage as basin fill alluvium or in fans, or too high due to extended surface exposure of sediments that are

rarely transported (e.g. Clapp et al., 2002; Ritter et al., 2023). This is further complicated by insufficient mixing of sediments from different parts of the catchments, as has been found for other dry regions (e.g. Clapp et al., 2002). Such biases could contribute to the variability in erosion rates we observe between proximal sites. However, catchments NG-C3 and NG-C4 show much more consistent rates between individual subcatchments, suggesting headwater catchment erosion rates on the order of $\sim 1\text{--}3 \text{ m Ma}^{-1}$ are typical in this region of the Coastal Cordillera.

6.4. Regional and global perspectives

The exceptional preservation of fault scarps in our study area reflects the sharp climatic gradient across the Coastal Cordillera, which delineates contrasting erosional regimes on its western and eastern flanks (eg. Hartley et al., 2005; Bartz et al., 2020). Along the coast, fog-derived moisture, ENSO-related rainfall, and marine influence promote weathering, salt-induced disintegration of clasts, and episodic sediment supply to active alluvial fans. In contrast, the western Central Depression lies beyond the direct reach of these processes, with minimal sediment availability and surface activity. The persistence of hyperarid conditions inland has therefore limited denudation, allowing scarps and associated geomorphic markers to remain sharply defined over Quaternary

timescales. Similar gradients have also been documented further north in the Coastal Cordillera, where cosmogenic nuclide-derived erosion rates increase more than an order of magnitude over short distances, reflecting the interplay between fog distribution, wind exposure, and the presence or absence of gypsum–halite ground cover (Mohren et al., 2020). This comparison reinforces that preservation in our study area is fundamentally climate-driven, governed by localized moisture inputs that determine whether salts act as erosive agents or as long-term stabilizers of geomorphic surfaces.

Fault scarp preservation in our study is not unique to northern Chile but part of a broader pattern observed in other arid regions such as southern Peru (Benavente et al., 2017), Negev Desert in Israel (Begin, 1992; Enzel et al., 1996), and Namib Desert in Namibia (Muir et al., 2023), where Quaternary faulting has also produced remarkable well-preserved landforms. However, the hyperarid conditions of the Atacama Desert represent one of the most extreme cases globally. Erosion rates in this region are exceptionally low, as evinced by the rates we measure here and from other studies. Such rates are comparable only to other hyperarid environments such as the southern Negev Desert, where abandoned alluvial surfaces have been reported to erode at rates as low as $0.25\text{--}0.3 \text{ m My}^{-1}$ (Matmon et al., 2009). Other arid deserts, such as the Namib, report erosion rates, with values ranging from 3 to 9 m My^{-1} in large river systems (Bierman and Caffee, 2001). This suggests that hyperaridity, combined with low tectonic slip rates ($\sim 0.07 \text{ mm yr}^{-1}$) generate a preservation window far longer than typical in semi-arid zones. In our case study, moisture inputs are minimal but significant in the form of coastal fog, which contributes to the formation of gypsic soil and the cementation/stabilization of alluvial surfaces and fault scarps (Butler, 1980). The gypsic soils we document (Gs1, Gs2) are crucial for stabilizing post-faulting colluvial deposits, reducing susceptibility to erosion. Similar gypsic horizons in other arid regions (e.g., Eckardt et al., 2001; Aref, 2003; Amit and Yaalon, 1996) form over timescales of $10^4\text{--}10^5$ years under negative water balance, consistent with the long-term preservation. In our study area the soils formed during longer time scales, probably exceeding 10^6 years. Furthermore, the slow conversion of gypsum to anhydrite under surface conditions highlights the long-term geochemical stability of these soils and their influence on the observed geomorphic persistence. This process parallels pedogenic stabilization observed in other coastal regions such as the Namib Desert where fog-driven moisture facilitates the precipitation of gypsum influencing sediment redistribution, geomorphic stabilization (Eckardt and Spiro, 1999) and the local variability of scarp degradation (Muir et al., 2023). Spatial gradients in fog, frequency, intensity and long-term variations likely influence the geomorphic stabilization of the landscape and determine the competition between tectonic slip rates and surface processes. In the Namib Desert, the sulphur incorporated into gypsum is largely supplied by atmospheric deposition of sulphates originating from decomposition of phytoplankton (Eckardt and Spiro, 1999). These sulphates are linked to high primary productivity in the Benguela upwelling system (Eckardt and Spiro, 1999). Similar conditions could prevail in the Atacama Desert where offshore upwelling process is associated with the Humboldt current (Thiel et al., 2007; Garreaud et al., 2009, 2010). It underscores the need to integrate oceanic and atmospheric dynamics into landscape evolution models.

6.5. Conceptual model and implications

We propose a conceptual model in which extremely low erosion rates, sporadic but effective hydrologic events, and salt-cemented soils collectively inhibit rapid degradation, enabling fault scarps to persist for tens of thousands of years. This deviates from classic scarp evolution models (e.g., Nash, 1980; Hanks and Wallace, 1985; Bucknam and Anderson, 1978) developed for semi-arid or temperate regions. Our findings indicate that, in tectonically active but hyperarid landscapes, fault scarps can serve as reliable markers of late Quaternary deformation, highlighting the importance of incorporating climate–soil–tectonic

feedback into landscape evolution frameworks. The extraordinary preservation of tectonic landforms in our study results from the combined effects of (i) hyperarid climate, (ii) sporadic but effective hydrologic events, (iii) low slip rates, and (iv) cementation by salts. This system challenges classical models of scarp evolution and highlights the need to explicitly incorporate climate–soil–tectonic interactions in landscape evolution frameworks.

7. Conclusions

This study provides insights into the long-term preservation of fault scarps in the hyperarid Atacama Desert, particularly within the Atacama Fault System (AFS) of northern Chile. Despite a slow fault slip rate ($\sim 0.07 \text{ mm yr}^{-1}$), fault morphologies (e.g., free faces and colluvial wedges) have remained preserved for tens of thousands of years. Sustained hyperaridity since the Late Pleistocene is the primary factor controlling this preservation.

Our findings indicate that scarp degradation in this region is associated with exceptionally low diffusion coefficients, as calculated for the Salar del Carmen scarp ($k = 0.063 \pm 0.018 \text{ m}^2 \text{ ka}^{-1}$) and localized channel incisions, likely triggered by infrequent, intense rainfall events. Minimal but significant moisture input from coastal fog promotes gypsic soil formation, enhancing moisture retention and driving gypsum cementation that stabilizes alluvial surfaces and prevents free face collapse.

Furthermore, morphometric analysis using the Ds index revealed minimal along-strike degradation in areas such as Salar del Carmen and Naguayán, which aligns with the low catchment erosion rates calculated ($\sim 0.5\text{--}2.9 \text{ m Ma}^{-1}$). These results challenge conventional scarp degradation models based on arid environments, suggesting that free-face persistence can serve as a reliable proxy for long-term tectonic activity in hyperarid settings.

We propose a conceptual model in which the combined effects of (i) a hyperarid climate, (ii) sporadic but geomorphically effective hydrologic events, (iii) low tectonic slip rates, and (iv) salt-induced cementation act together to inhibit scarp degradation. This model enhances our understanding of fault activity in arid tectonic settings and carries important implications for interpreting landscape evolution and assessing seismic hazard in hyperarid regions.

Author contributions

P. Rivera carried out the geomorphic mapping, morphometric analyses, soil and sediment studies, and prepared the original draft. G. González provided expertise in active tectonics, paleoseismology, and earthquake geology, and contributed with supervision, resources, and funding acquisition. S.A. Binnie supervised and contributed to the laboratory processing and analysis of cosmogenic nuclides. All authors discussed the results and contributed to the final manuscript.

Declaration of competing interest

The authors declare that they have no known competing financial interests or personal relationships that could have appeared to influence the work reported in this paper.

Acknowledgement

We thank FONDECYT project 1200170 for funding fieldwork and covering analytical costs, the National Research Center for Integrated Natural Disaster Management (CIGIDEN) through CONICYT/FONDAP project 1523A0009, and the ANID PhD grant 21200521 supported by the Chilean Government. Binnie acknowledges support from the Deutsche Forschungsgemeinschaft (DFG, German Research Foundation) – Projektnummer 268236062 – SFB 1211. We also thank the X-ray Diffraction Laboratory of the Department of Geology at the Universidad

Católica del Norte and Damian Lopez and Elena Voronina from the Cosmogenic Nuclide Laboratory of the University of Cologne, Germany, for their technical support and collaboration. We are grateful to the two anonymous reviewers whose constructive comments and suggestions helped improve the clarity and scope of this work.

Appendix A. Supplementary data

Supplementary data to this article can be found online at <https://doi.org/10.1016/j.quascirev.2025.109627>.

Data availability

All data and/or code is contained within the submission.

References

- Allmendinger, R., González, G., 2010. Neogene to Quaternary tectonics of the coastal Cordillera, northern Chile. *Tectonophysics* 495 (1–2), 93–110. <https://doi.org/10.1016/j.tecto.2009.04.019>.
- Amit, R., Harrison, J.B.J., Enzel, Y., 1995. Use of soils and colluvial deposits in analyzing tectonic events in the southern Arava Rift, Israel. *Geomorphology* 12, 91–107. [https://doi.org/10.1016/0169-555X\(94\)00081-2](https://doi.org/10.1016/0169-555X(94)00081-2).
- Amit, R., Yaalon, D.H., 1996. The micromorphology of gypsum and halite in Reg soils—The Negev Desert, Israel. *Earth Surf. Process. Landf.* 21 (12), 1127–1143. [https://doi.org/10.1002/\(SICI\)1096-9837\(199612\)21:12<1127::AID-ESP656>3.0.CO;2-G](https://doi.org/10.1002/(SICI)1096-9837(199612)21:12<1127::AID-ESP656>3.0.CO;2-G).
- Amundson, R., Dietrich, W., Bellugi, D., Ewing, S., Nishiizumi, K., Chong, G., Owen, J., Finkel, R., Heimsath, A., Stewart, B., Caffee, M., 2012. Geomorphologic evidence for the late Pliocene onset of hyperaridity in the Atacama Desert. *Geol. Soc. Am. Bull.* 124 (7–8), 1048–1070. <https://doi.org/10.1130/B30445.1>.
- Arabasz, W.J., 1971. Geological and Geophysical Studies of the Atacama Fault System in Northern Chile. PhD thesis, Calif. Inst. Technol., Pasadena, p. 264.
- Aref, M.A.M., 2003. Classification and depositional environments of Quaternary pedogenic gypsum crusts (gypcrete) from east of the Fayum depression, Egypt. *Sediment. Geol.* 155 (1–2), 87–108. [https://doi.org/10.1016/S0037-0738\(02\)00162-8](https://doi.org/10.1016/S0037-0738(02)00162-8).
- Balco, G., Stone, J.O., Lifton, N.A., Dunai, T.J., 2008. A complete and easily accessible means of calculating surface exposure ages or erosion rates from ¹⁰Be and ²⁶Al measurements. *Quat. Geochronol.* 3, 174–195. <https://doi.org/10.1016/j.quageo.2007.12.001>.
- Bartz, M., Walk, J., Binnie, S.A., Brill, D., Stauch, G., Lehmkuhl, F., Hoffmeister, D., Brückner, H., 2020. Late Pleistocene alluvial fan evolution along the coastal Atacama Desert (N Chile). *Glob. Planet. Change* 190, 103091. <https://doi.org/10.1016/j.gloplacha.2019.103091>.
- Begin, Z.B., 1992. Application of quantitative morphological dating to paleo-seismicity of the northwestern Negev, Israel. *J. Earth Sci.* 41, 95–103.
- Benavente, C., Zerathe, S., Audin, L., Hall, S.R., Robert, X., Delgado, F., Carcaillet, J., ASTER Team, 2017. Active transpressional tectonics in the Andean forearc of southern Peru quantified by ¹⁰Be surface exposure dating of an active fault scarp. *Tectonics* 36, 1662–1678. <https://doi.org/10.1002/2017TC004523>.
- Binnie, S.A., Phillips, W.M., Summerfield, M.A., Fifield, L.K., 2006. Sediment mixing and basin-wide cosmogenic nuclide analysis in rapidly eroding mountainous environments. *Quat. Geochronol.* 1 (1), 4–14. <https://doi.org/10.1016/j.quageo.2006.06.013>.
- Bierman, P.R., Steig, E.J., 1996. Estimating rates of denudation using cosmogenic isotope abundances in sediment. *Earth Surf. Process. Landf.* 21, 125–139. [https://doi.org/10.1002/\(SICI\)1096-9837\(199612\)21:12<125::AID-ESP656%3E3.0.CO;2-G](https://doi.org/10.1002/(SICI)1096-9837(199612)21:12<125::AID-ESP656%3E3.0.CO;2-G).
- Bierman, P.R., Caffee, M., 2001. Slow rates of rock surface erosion and sediment production across the Namib Desert and escarpment, Southern Africa. *Am. J. Sci.* 301 (4–5), 326–358. <https://doi.org/10.2475/ajs.301.4-5.326>.
- Birkeland, P.W., 1999. Soils and Geomorphology, third ed. Oxford Univ. Press, New York.
- Böhm, C., Reyers, M., Knarr, L., Crewell, S., 2021. The role of moisture conveyor belts for precipitation in the Atacama Desert. *Geophys. Res. Lett.* 48 (24), e2021GL094372. <https://doi.org/10.1029/2021GL094372>.
- Bozkurt, D., Rondonelli, R., Garreaud, R., Arriagada, A., 2016. Impact of warmer eastern tropical Pacific SST on the March 2015 Atacama floods. *Mon. Weather Rev.* 144 (11), 4441–4460. <https://doi.org/10.1175/MWR-D-16-0041.1>.
- Buchun, Z., Yuhua, L., Shunmin, G., Wallace, R.E., Bucknam, R.C., Hanks, T.C., 1986. Fault scarps related to the 1739 earthquake and seismicity of the Yinchuan graben, Ningxia Huizu Zizhiqu, China. *Bull. Seismol. Soc. Am.* 76, 1253–1287. <https://doi.org/10.1785/BSSA0760051253>.
- Bucknam, R.C., Anderson, R.E., 1978. Estimation of fault-scarp ages from a scarp-height-slope-angle relationship. *Geology* 7, 11–14. [https://doi.org/10.1130/0091-7613\(1979\)7<11:EOFABA>2.0.CO;2](https://doi.org/10.1130/0091-7613(1979)7<11:EOFABA>2.0.CO;2).
- Butler, B.E., 1980. Soil Classification for Soil Survey. Clarendon Press, Oxford; Oxford University Press, New York, p. 129.
- Carretier, S., Tolorza, V., Regard, V., Aguilar, G., Bermúdez, M.A., Martinod, J., Guyot, J.-L., Héral, G., Riquelme, R., 2018. Review of erosion dynamics along the major N-S climatic gradient in Chile and perspectives. *Geomorphology* 300, 45–68. <https://doi.org/10.1016/j.geomorph.2017.10.016>.
- Caskey, S.J., Wesnousky, S.G., Zhang, P., Slemmons, D.B., 1996. Surface faulting of the 1954 Fairview Peak (M_w 7.2) and Dixie Valley (M_w 6.8) earthquakes, central Nevada. *Bull. Seismol. Soc. Am.* 86, 761–787. <https://doi.org/10.1785/BSSA0860030761>.
- Cereceda, P., Larraín, H., Osses, P., Farías, M., Egaña, I., 2008. The climate of the coast and fog zone in the Tarapacá Region, Atacama Desert, Chile. *Atmos. Res.* 87, 301–311. <https://doi.org/10.1016/j.atmosres.2007.11.011>.
- Chen, K., Milliner, C., Avouac, J.-P., 2019. The Weitin fault, Papua New Guinea, ruptured twice by Mw 8.0 and Mw 7.7 earthquakes in 2000 and 2019. *Geophys. Res. Lett.* 46, 12833–12840. <https://doi.org/10.1029/2019GL084645>.
- Clapp, E.M., Bierman, P.R., Caffee, M., 2002. Using ¹⁰Be and ²⁶Al to determine sediment generation rates and identify sediment source areas in an arid region drainage basin. *Geomorphology* 45 (1–2), 89–104. [https://doi.org/10.1016/S0169-555X\(01\)00191-X](https://doi.org/10.1016/S0169-555X(01)00191-X).
- Cortés, J., Marquardt, C., González, G., Wilke, H., Marinovic, N., 2007. Carta Mejillones Y Península De Mejillones, Región De Antofagasta. Carta Geológica De Chile, Serie Geología Básica, 1 Mapa Escala 1:100,000. Servicio Nacional de Geología y Minería.
- Cortés, J., González, G., Binnie, S.A., Robinson, R., Freeman, S., Vargas, G., 2012. Paleoseismology of the Mejillones fault, northern Chile: insights from cosmogenic ¹⁰Be and optically stimulated luminescence determinations. *Tectonics* 31, TC2017.
- De Pascale, G.P., Chandler-Yates, N., Dela Pena, F., Wilson, P., May, E., Twiss, A., Cheng, C., 2016. Active tectonics west of New Zealand's Alpine fault: South Westland Fault Zone activity shows Australian Plate instability. *Geophys. Res. Lett.* 43, 3120–3125. <https://doi.org/10.1002/2016GL068233>.
- Del Río, I., Sawakuchi, A.O., González, G., 2019. Luminescence dating of sediments from central Atacama Desert, northern Chile. *Quat. Geochronol.* 53, 101002. <https://doi.org/10.1016/j.quageo.2019.05.001>.
- Delouis, B., Cisternas, A., Dorbath, L., Rivera, L., Kausel, E., 1996. The Andean subduction zone between 22°S and 24°S (northern Chile): precise geometry and states of stress. *Tectonophysics* 259, 81–100. [https://doi.org/10.1016/0040-1951\(95\)00065-8](https://doi.org/10.1016/0040-1951(95)00065-8).
- Delouis, B., Philip, H., Dorbath, L., Cisternas, A., 1998. Recent crustal deformation in the Antofagasta region (northern Chile) and the subduction process. *Geophys. J. Int.* 132, 302–338. <https://doi.org/10.1046/j.1365-246x.1998.00439.x>.
- DiBiase, R.A., 2018. Short communication: increasing vertical attenuation length of cosmogenic nuclide production on steep slopes negates topographic shielding corrections for catchment erosion rates. *Earth Surf. Dynam.* 6, 923–931. <https://doi.org/10.5194/esurf-6-923-2018>.
- Diederich, J.L., Wennrich, V., Bao, R., Büttner, C., Bolten, A., Brill, D., Buske, S., Campos, E., Fernández-Galego, E., Gödickmeier, P., Ninnemann, L., Reyers, M., Ritter, B., Ritterbach, L., Rolf, C., Scheidt, S., Dunai, T.J., Melles, M., 2020. A 68 ka precipitation record from the hyperarid core of the Atacama Desert in northern Chile. *Global Planet. Change* 184, 103054. <https://doi.org/10.1016/j.gloplacha.2019.103054>.
- Dunai, T.J., González López, G.A., Juez-Larré, J., 2005. Oligocene–Miocene age of aridity in the Atacama Desert revealed by exposure dating erosion-sensitive landforms. *Geology* 33, 321–324. <https://doi.org/10.1130/G21184.1>.
- DuRoss, B., Briggs, R.W., Gold, R.D., Hatem, A.E., Elliott, A.J., Delano, J., Medina-Cascales, I., Gray, H.J., Mahan, S.A., Nicovich, S.R., Lifton, Z.M., Kleber, E., McDonald, G., Hiscock, A., Bunds, M., Reitman, N.G., 2022. How similar was the 1983 Mw 6.9 Borah Peak earthquake rupture to its surface-faulting predecessors along the northern Lost River fault zone (Idaho, USA)? *Geol. Soc. Am. Bull.* 134, 2767–2789. <https://doi.org/10.1130/B36144.1>.
- Eckardt, F.D., Spiro, B., 1999. The origin of sulphur in gypsum and dissolved sulphate in the Central Namib Desert, Namibia. *Sediment. Geol.* 123, 255–273. [https://doi.org/10.1016/S0037-0738\(98\)00137-7](https://doi.org/10.1016/S0037-0738(98)00137-7).
- Eckardt, F.D., Drake, N., Goudie, A.S., White, K., Viles, H., 2001. The role of playas in pedogenic gypsum crust formation in the Central Namib Desert: a theoretical model. *Earth Surf. Process. Landf.* 26, 1177–1193. <https://onlinelibrary.wiley.com/doi/10.1002/esp.264>.
- Enzel, Y., Amit, R., Porat, N., Zilberman, E., Harrison, B.J., 1996. Estimating the ages of fault scarps in the Arava, Israel. *Tectonophysics* 253, 305–317. [https://doi.org/10.1016/0040-1951\(95\)00072-0](https://doi.org/10.1016/0040-1951(95)00072-0).
- Evenstar, L.A., Mather, A.E., Hartley, A.J., Stuart, F.M., Sparks, R.S.J., Cooper, F.J., 2017. Geomorphology on geologic timescales: evolution of the late Cenozoic Pacific paleosurface in Northern Chile and Southern Peru. *Earth Sci. Rev.* 171, 1–27. <https://doi.org/10.1016/j.earscirev.2017.04.004>.
- Ewiak, O., Victor, P., Oncken, O., 2015. Investigating multiple fault rupture at the Salar del Carmen segment of the Atacama Fault System (northern Chile): fault scarp morphology and knickpoint analysis. *Tectonics* 34, 187–212. <https://doi.org/10.1002/2014TC003599>.
- Ewing, S.A., Sutter, B., Owen, J., Nishiizumi, K., Sharp, W., Cliff, S.S., Perry, K., Dietrich, W., McKay, C.P., Amundson, R., 2006. A threshold in soil formation at Earth's arid–hyperarid transition. *Geochem. Cosmochim. Acta* 70 (21), 5293–5322. <https://doi.org/10.1016/j.gca.2006.08.020>.
- Garreaud, R.D., Vuille, M., Compagnucci, R., Marengo, J., 2009. Present-day South American climate. *Palaeogeogr. Palaeoclimatol. Palaeoecol.* 281 (3–4), 180–195. <https://doi.org/10.1016/j.palaeo.2007.10.032>.
- Garreaud, R.D., Molina, A., Farías, M., 2010. Andean uplift, ocean cooling and Atacama hyperaridity: a climate modeling perspective. *Earth Planet Sci. Lett.* 292 (1–2), 39–50. <https://doi.org/10.1016/j.epsl.2010.01.017>.
- Gerson, R., Grossman, S., Amit, R., Greenbaum, N., 1993. Indicators of faulting events and periods of quiescence in desert alluvial fans. *Earth Surf. Process. Landf.* 18, 181–202. <https://doi.org/10.1002/esp.3290180303>.

- González, G., Carrizo, D., 2003. Segmentación, cinemática y cronología relativa de la deformación tardía de la Falla Salar del Carmen, Sistema de Fallas de Atacama, Cordillera de la Costa de Antofagasta. Rev. Geol. Chile 30, 223–244. <https://doi.org/10.4067/S0716-02082003000200005>.
- González, G., Cembrano, J., Carrizo, D., Macci, A., Schneider, H., 2003. Link between forearc tectonics and Pliocene–Quaternary deformation of the Coastal Cordillera, northern Chile. J. S. Am. Earth Sci. 16, 321–342. [https://doi.org/10.1016/S0895-9811\(03\)00100-7](https://doi.org/10.1016/S0895-9811(03)00100-7).
- González, G., Dunai, T., Carrizo, D., Allmendinger, R., 2006. Young displacements on the Atacama Fault System, Northern Chile from field observations and cosmogenic ^{21}Ne concentrations. Tectonics 25 (4), TC4006. <https://doi.org/10.1029/2005TC001846>.
- González, G., Astudillo-Sotomayor, L., Del Río, I., Sawakuchi, A.O., Amidon, W., 2025. Tracing the relationship between the upper plate earthquake cycle and megathrust slip, the Atacama fault system in northern Chile. Sci. Rep. 15, 2914. <https://doi.org/10.1038/s41598-025-86877-0>.
- Goudie, A.S., Wright, E., Viles, H.A., 2002. The roles of salt (sodium nitrate) and fog in weathering: a laboratory simulation of conditions in the northern Atacama Desert, Chile. Catena 48, 255–266. [https://doi.org/10.1016/S0341-8162\(02\)00028-0](https://doi.org/10.1016/S0341-8162(02)00028-0).
- Granger, D.E., Kirchner, J.W., Finkel, R., 1996. Spatially averaged long-term erosion rates measured from in situ-produced cosmogenic nuclides in alluvial sediment. J. Geol. 104, 249–257. <https://doi.org/10.1086/629823>.
- Gray, H., DuRoss, C., Nicovich, S., Gold, R., 2022. Luminescence sediment tracing reveals the complex dynamics of colluvial wedge formation. Sci. Adv. 8, eab0747. <https://doi.org/10.1126/sciadv.abo0747>.
- Hanks, T.C., Wallace, R.E., 1985. Morphological analysis of the Lake Lahontan shoreline and beachfront fault scarps, Pershing County, Nevada. Bull. Seismol. Soc. Am. 75, 835–846. <https://doi.org/10.1785/BSSA0770030835>.
- Hanks, T.C., Schwartz, D.P., 1987. Morphologic dating of the pre-1983 fault scarp on the Lost River fault at Doublespring Pass Road, Custer County, Idaho. Bull. Seismol. Soc. Am. 77, 837–846. <https://doi.org/10.1785/BSSA0770030837>.
- Hartley, A.J., Jolley, E.J., 1995. Tectonic implications of late Cenozoic sedimentation from the Coastal Cordillera of northern Chile (22°–24°S). J. Geol. Soc. Lond. 152, 51–63. <https://doi.org/10.1144/gsjgs.152.1.0051>.
- Hartley, A.J., Mather, A.E., Jolley, E., Turner, P., 2005. Climatic controls on alluvial-fan activity, Coastal Cordillera, northern Chile. Geol. Soc. Lond., Spec. Publ. 251, 95–116. <https://doi.org/10.1144/gsl.sp.2005.251.01.08>.
- Herrero, J., Porta, J., 2000. The terminology and the concepts of gypsum-rich soils. Geoderma 96, 47–61. [https://doi.org/10.1016/S0016-7061\(00\)00003-3](https://doi.org/10.1016/S0016-7061(00)00003-3).
- Houston, J., Hartley, A.J., 2003. The central Andean west-slope rainshadow and its potential contribution to the origin of hyper-aridity in the Atacama Desert. Int. J. Climatol. 23, 1453–1464. <https://doi.org/10.1002/joc.938>.
- Houston, J., 2006. Variability of precipitation in the Atacama Desert: its causes and hydrological impact. Int. J. Climatol. 26, 2181–2198. <https://doi.org/10.1002/joc.1359>.
- Johnson, K.L., Nissen, E., Lajoie, L., 2018. Surface rupture morphology and vertical slip distribution of the 1959 Mw 7.2 Hebgen Lake (Montana) earthquake from airborne lidar topography. J. Geophys. Res. Solid Earth 123, 8229–8248. <https://doi.org/10.1029/2017JB015039>.
- Jungers, M.C., Heimsath, A.M., Amundson, R., Balco, G., Shuster, D., Chong, G., 2013. Active erosion–deposition cycles in the hyperarid Atacama Desert of Northern Chile. Earth Planet Sci. Lett. 371–372, 125–133. <https://doi.org/10.1016/j.epsl.2013.04.005>.
- Kogan, L., Bendick, R., 2011. A mass failure model for the initial degradation of fault scarps, with application to the 1959 scarps at Hebgen Lake, Montana. Bull. Seismol. Soc. Am. 101 (1), 68–78. <https://doi.org/10.1785/0120100107>.
- Lifton, N., Sato, T., Dunai, T.J., 2014. Scaling in situ cosmogenic nuclide production rates using analytical approximations to atmospheric cosmic-ray fluxes. Earth Planet Sci. Lett. 386, 149–160. <https://doi.org/10.1016/j.epsl.2013.10.052>.
- McCalpin, J.P., 2009. Paleoseismology. In: Int. Geophys. 95, second ed. Academic Press, Burlington, Mass, p. 613.
- McFadden, L.D., Wells, S.G., Eppes, M.C., Gillespie, A.R., 2000. The evolution of desert piedmont surfaces: studies of the origin of desert pavements and soils. Geol. Soc. Am. Abstr. Programs 32 (7), 222.
- Matmon, A., Simhai, O., Amit, R., Haviv, I., Porat, N., McDonald, E., Benedetti, L., Finkel, R., 2009. Desert pavement-coated surfaces in extreme deserts present the longest-lived landforms on Earth. Geol. Soc. Am. Bull. 121 (5–6), 688–697. <https://doi.org/10.1130/B26422.1>.
- Mohren, J., Binnie, S.A., Ritter, B., Dunai, T.J., 2020. Development of a steep erosional gradient over a short distance in the hyperarid core of the Atacama Desert, Northern Chile. Glob. Planet. Change 184, 103068. <https://doi.org/10.1016/j.gloplacha.2019.103068>.
- Montgomery, D.R., Balco, G., Willett, S.D., 2001. Climate, tectonics, and the morphology of the Andes. Geology 29, 579–582. [https://doi.org/10.1130/0091-7613\(2001\)029%3C0579:CTATMO%3E2.0.CO;2](https://doi.org/10.1130/0091-7613(2001)029%3C0579:CTATMO%3E2.0.CO;2).
- Muir, R.A., Whitehead, B., New, T., Stevens, V., Macey, P.H., Groenewald, C.A., et al., 2023. Exceptional scarp preservation in SW Namibia reveals geological controls on large magnitude intraplate seismicity in southern Africa. Tectonics 42, e2022TC007693. <https://doi.org/10.1029/2022TC007693>.
- Naranjo, J., 1987. Interpretación de la actividad cenozoica superior a lo largo de la Zona de Fallas de Atacama, norte de Chile. Rev. Geol. Chile 31, 43–55.
- Nash, D.B., 1980. Morphologic dating of degraded normal fault scarps. J. Geol. 88, 353–360. <https://doi.org/10.1086/628513>.
- Nichols, K.K., Bierman, P.R., Hooke, R.L., Clapp, E.M., Caffee, M., 2002. Quantifying sediment transport on desert piedmonts using Be-10 and Al-26. Geomorphology 45, 105–125. [https://doi.org/10.1016/S0169-555X\(01\)00192-1](https://doi.org/10.1016/S0169-555X(01)00192-1).
- Niemeyer, H., González, G., Martínez-De Los Ríos, E., 1996. Evolución tectónica cenozoica del margen continental activo de Antofagasta, norte de Chile. Rev. Geol. Chile 23, 165–186.
- Norton, K., Schlunegger, F., 2011. Migrating deformation in the Central Andes from enhanced orographic rainfall. Nat. Commun. 2, 584. <https://doi.org/10.1038/ncomms1590>.
- Pierce, K.L., Colman, S.M., 1986. Effect of height and orientation (microclimate) on geomorphic degradation rates and processes, late-glacial terrace scarps in Central Idaho. Geol. Soc. Am. Bull. 97, 869–885. [https://doi.org/10.1130/0016-7606\(1986\)97<869:EOHAM>2.0.CO;2](https://doi.org/10.1130/0016-7606(1986)97<869:EOHAM>2.0.CO;2).
- Placzek, C.J., Matmon, A., Granger, D.E., Quade, J., Niedermann, S., 2010. Evidence for active landscape evolution in the hyperarid Atacama from multiple terrestrial cosmogenic nuclides. Earth Planet Sci. Lett. 295, 12–20. <https://doi.org/10.1016/j.epsl.2010.03.006>.
- Rech, J.A., Quade, J., Hart, W.S., 2003. Isotopic evidence for the source of Ca and S in soil gypsum, anhydrite and calcite in the Atacama Desert, Chile. Geochim. Cosmochim. Acta 67, 575–586. [https://doi.org/10.1016/S0016-7037\(02\)01175-4](https://doi.org/10.1016/S0016-7037(02)01175-4).
- Rech, J.A., Currie, B.S., Shullenberger, E.D., Dunagan, S.P., Jordan, T.E., Blanco, N., Tomlinson, A.J., Rowe, H.D., Houston, J., 2010. Evidence for the development of the Andean rain shadow from a Neogene isotopic record in the Atacama Desert, Chile. Earth Planet Sci. Lett. 292, 371–382. <https://doi.org/10.1016/j.epsl.2010.02.004>.
- Rech, J.A., Currie, B.S., Jordan, T.E., Riquelme, R., Lehmann, S.B., Kirk-Lawlor, N.E., Li, S., Gooley, J.T., 2019. Massive middle Miocene gypsiferous paleosols in the Atacama Desert and the formation of the Central Andean rain-shadow. Earth Planet Sci. Lett. 506, 184–194. <https://doi.org/10.1016/j.epsl.2018.10.040>.
- Reyers, M., Fiedler, S., Ludwig, P., Böhm, C., Wennrich, V., Shao, Y., 2023. On the importance of moisture conveyor belts from the tropical eastern Pacific for wetter conditions in the Atacama Desert during the mid-Pliocene. Clim. Past 19 (2), 517–532. <https://doi.org/10.5194/cp-19-517-2023>.
- Ritter, B., Stuart, F.M., Binnie, S.A., Gerdes, A., Wennrich, V., Dunai, T.J., 2018. Neogene fluvial landscape evolution in the hyperarid core of the Atacama Desert. Sci. Rep. 8, 13952. <https://doi.org/10.1038/s41598-018-32339-9>.
- Ritter, B., Wennrich, V., Medialdea, A., Brill, D., King, G., Schneiderwind, S., Niemann, K., Fernández-Galego, E., Diederich, J., Rolf, C., Bao, R., Melles, M., Dunai, T.J., 2019. Climatic fluctuations in the hyperarid core of the Atacama Desert during the past 215 ka. Sci. Rep. 9, 5270. <https://doi.org/10.1038/s41598-019-41743-8>.
- Ritter, B., Mohren, J., Binnie, S.A., Wennrich, V., Dunkl, I., Albert, R., Gerdes, A., LoBue, S., Dunai, T.J., 2023. Shaping the Huara Intrusive Complex in the hyperarid Atacama Desert—Erosional near-stasis contrasting high topographic gradients. J. Geophys. Res. Earth Surf. 128 (3), e2022JF006986. <https://doi.org/10.1029/2022JF006986>.
- Scheuber, E., Andriessen, P.M., 1990. The kinematic significance of the Atacama Fault Zone, Northern Chile. J. Struct. Geol. 12, 243–257. [https://doi.org/10.1016/0191-8141\(90\)90008-M](https://doi.org/10.1016/0191-8141(90)90008-M).
- Scheuber, E., González, G., 1999. Tectonics of the Jurassic–Early Cretaceous magmatic arc of the north Chilean Coastal Cordillera (22°–26°S): a story of crustal deformation along a convergent plate boundary. Tectonics 18, 895–910. <https://doi.org/10.1029/1999TC900024>.
- Schwanghart, W., Scherler, D., 2014. TopoToolbox 2 – matlab-based software for topographic analysis and modeling in Earth surface sciences (version 2.0). Earth Surf. Dyn. Software. <https://doi.org/10.5194/esurf-2-1-2014>.
- Suter, M., 2015. Rupture of the Pitáyacachi Fault in the 1887 Mw 7.5 Sonora, Mexico earthquake (southern basin-and-range Province): rupture kinematics and epicenter inferred from rupture branching patterns. J. Geophys. Res. Solid Earth 120, 617–641. <https://doi.org/10.1002/2014JB011244>.
- Thiel, M., Macaya, E.C., Acuña, E., Arntz, W.E., Bastias, H., Brokordt, K., Camus, P.A., Castilla, J.C., Castro, L.R., Cortés, M., Dumont, C.P., Escribano, R., Fernandez, M., Gajardo, J.A., Gaymer, C.F., Gomez, I., González, A.E., González, H.E., Haye, P.A., et al., 2007. The Humboldt Current System of northern and central Chile – oceanographic processes, ecological interactions and socioeconomic feedback. Oceanogr. Mar. Biol. 45, 195–344.
- Voigt, C., Klipsch, S., Herzwart, D., Chong, G., Staubwasser, M., 2020. The spatial distribution of soluble salts in the surface soil of the Atacama Desert and their relationship to hyperaridity. Glob. Planet. Change 184, 103077. <https://doi.org/10.1016/j.gloplacha.2019.103077>.
- Wallace, R.E., 1977. Profiles and ages of young fault scarps, north-central Nevada. Geol. Soc. Am. Bull. 88 (9), 1267–1281. [https://doi.org/10.1130/0016-7606\(1977\)88%3C1267:PAOY%3E2.0.CO;2](https://doi.org/10.1130/0016-7606(1977)88%3C1267:PAOY%3E2.0.CO;2).
- Wallace, R.E., 1980. Degradation of the Hebgen Lake fault scarps of 1959. Geology 8 (5), 225–229. [https://doi.org/10.1130/0091-7613\(1980\)8<225:DOTHLF>2.0.CO;2](https://doi.org/10.1130/0091-7613(1980)8<225:DOTHLF>2.0.CO;2).
- Wang, F., Michalski, G., Seo, J.H., Ge, W.S., 2014. Geochemical, isotopic, and mineralogical constraints on atmospheric deposition in the hyper-arid Atacama Desert, Chile. Geochim. Cosmochim. Acta 135, 29–48. <https://doi.org/10.1016/j.gca.2014.03.017>.
- Wara, M.W., Ravelo, A.C., Delaney, M.L., 2005. Permanent El Niño-like conditions during the Pliocene warm period. Science 309, 758–761. <https://doi.org/10.1126/science.1112596>.